

# Pairing effects on pure rotational energy of nuclei

K. Abe

*Department of Physics, Graduate School of Science and Engineering,  
Chiba University, Yayoi-cho 1-33, Inage, Chiba 263-8522, Japan*

H. Nakada\*

*Department of Physics, Graduate School of Science,  
Chiba University, Yayoi-cho 1-33, Inage, Chiba 263-8522, Japan*

## Abstract

By applying the angular-momentum projection (AMP) to the self-consistent axial mean-field solutions with the semi-realistic effective Hamiltonian M3Y-P6, the pairing effects on the pure rotational energy of nuclei, *i.e.*, the rotational energy at a fixed intrinsic state, have been investigated. While it was shown at the Hartree-Fock (HF) level that the individual terms of the Hamiltonian contribute to the rotational energy with ratios insensitive to nuclides except for light or weakly-deformed nuclei, the pair correlations significantly change the contributions, even for the well-deformed heavy nuclei. The contribution of the interaction to the rotational energy is found to correlate well with the degree of proximity between nucleons, which is measured via the expectation value that two nucleons exist at the same position. While the nucleons slightly spread as the angular momentum increases at the HF level, accounting for the positive (negative) contribution of the attractive (repulsive) components of the interaction, the pair correlations reduce or invert the effect.

## I. INTRODUCTION

It is known that the rotational band appears in a number of nuclei, giving the excitation energy  $E_x(J^+) = J(J+1)/(2\mathcal{I})$  above the ground state (g.s.) [1, 2]. These energy spectra indicate that the intrinsic state of the nucleus is deformed and rotates with the moment of inertia (MoI)  $\mathcal{I}$ . From a microscopic standpoint, nuclei are well described in the self-consistent mean-field (MF) theories, such as the Hartree-Fock (HF) and the Hartree-Fock-Bogoliubov (HFB) approximations [3], and the deformed intrinsic states of nuclei are obtained as MF solutions in which the rotational symmetry is spontaneously broken. The Nambu-Goldstone (NG) mode is accompanied by symmetry breaking, and it restores the corresponding symmetry in energy eigenstates. The restoration of the rotational symmetry corresponds with a whole rotation of a deformed intrinsic state. The superposition of the degenerate intrinsic states along the NG mode derives the angular-momentum projection (AMP) [3–23]. The AMP accounts for the  $J(J+1)$  rule of the excitation energy under a reasonable approximation for well-deformed heavy nuclei [3–5, 7, 8, 10]. However, rotational spectra have also been observed in light nuclei including those far off the  $\beta$ -stability. It will

---

\* nakada@faculty.chiba-u.jp

deserve reinvestigating from a general perspective how the rotational energy of nuclei arises, not restricting ourselves to well-deformed heavy nuclei.

In classical mechanics, the rotational energy arises from the kinetic energy, proportional to  $\mathbf{J}^2/(2\mathcal{I})$  for a rigid rotor with the angular momentum  $\mathbf{J}$ , in which the distance between constituent particles is invariant. On the other hand, the above-mentioned rotational energy of nuclei should be formed from the effective Hamiltonian, including the nucleonic interaction. In the Thouless-Valatin formula for the MoI [24], which is derived from the random-phase approximation (RPA), the g.s. correlations due to the interaction are taken into account. In Ref. [23], we investigated the composition of the rotational energy of various nuclei by applying the AMP to the HF solutions. When the rotational energy is decomposed into contributions of the individual terms of the Hamiltonian, those of the central forces are sizable, although the kinetic energies carry the major part and are close to the rigid-rotor values. The ratios of the individual terms of the Hamiltonian to the total rotational energy are insensitive to nuclides and deformation, as long as they are well-deformed and not very light. In contrast, the ratios significantly depend on nuclei and deformation for light or weakly-deformed nuclei.

It is known that the pair correlations in nuclei significantly influence the rotational energy. Within the cranking model [3], the Belyaev formula [25] accounts for the reduction of the MoI compared with the Inglis formula [26] due to the pair correlations. Conversely, the pair correlations could be influenced by the rotation; the pair correlation is suppressed by the cranking effect accompanied by the breaking of the time-reversal symmetry, known as the Mottelson-Valatin effect [27].

The effects of the pair correlations on the rotational energy of nuclei are investigated in this paper, extending the study in Ref. [23]. The AMP is applied to the self-consistent solutions of the Bardeen-Cooper-Schrieffer approximation on top of the axial HF orbitals (HF+BCS) as well as the axial HFB solutions. The Michigan-three-range-Yukawa (M3Y)-type nucleonic interactions [28–30] have been developed for the self-consistent MF calculations. With phenomenological modification of the original M3Y interaction obtained from the  $G$ -matrix calculations [31–34], they may be regarded as *semi-realistic* effective interactions. They have been pointed out to be free from most of the instabilities in the nuclear matter response functions, which sometimes occur in other interactions [35]. The M3Y-P6 parameter-set is employed [29, 30], which well describes the magic numbers of nuclei over a

wide range of the nuclear chart [36] and the deformation of nuclei [37, 38].

In the present study, the AMP is applied to the MF wave functions obtained by self-consistent axial-MF calculations with the M3Y-P6 interaction, including the pair correlations. We restrict ourselves to the energies arising solely from the rotation of the MF solutions in the projection-after-variation (PAV) framework as in Ref. [23], which may be called *pure rotational energy*<sup>1</sup>, separating them from the counter effects of the rotation on the intrinsic states. It should be kept in mind that the pure rotational energy is not necessarily enough to describe the rotational spectra in actual nuclei [6], because the rotation may significantly affect the intrinsic state as handled in the cranking model [3, 6, 10] and the variation-after-projection (VAP) schemes [3].

The correlations of the spatial proximity between two neutrons (protons) have attracted interest as di-neutron (di-proton) correlations [39]. The spatial correlations between nucleons could be relevant to the contributions of the nucleonic interaction to the rotational energy, giving us an insight into why the interaction contributes.

## II. THEORETICAL FRAMEWORK AND NUMERICAL METHOD

### A. AMP and cumulant expansion

The AMP is the method by which an intrinsic state is projected on angular-momentum eigenstates [3]. We consider an axially-symmetric intrinsic state, which is an eigenstate of  $\hat{J}_z$  with the eigenvalue  $M = 0$ . The intrinsic state  $|\Phi_0\rangle$  is expanded by angular-momentum eigenstates  $|J0\rangle$ ,  $|\Phi_0\rangle = \sum_J |J0\rangle \langle J0|\Phi_0\rangle$ , where we omit indices other than  $J$  and  $M (= 0)$  for simplicity. The Wigner (small)  $d$  function [3, 40, 41] of the angle  $\beta$ ,  $d_{MK}^{(J)}(\beta) := \langle JM|e^{-i\hat{J}_y\beta}|JK\rangle$ , takes a real number under the standard phase convention. The expectation values of the scalar operator  $\hat{\mathcal{S}}$  on the angular-momentum eigenstates are obtained as follows [3, 23]:

$$\langle J|\hat{\mathcal{S}}|J\rangle = \frac{\int_0^{\pi/2} d\beta \sin \beta d_{00}^{(J)}(\beta) \langle \Phi_0|\hat{\mathcal{S}} e^{-i\hat{J}_y\beta}|\Phi_0\rangle}{\int_0^{\pi/2} d\beta \sin \beta d_{00}^{(J)}(\beta) \langle \Phi_0|e^{-i\hat{J}_y\beta}|\Phi_0\rangle}. \quad (1)$$

---

<sup>1</sup> Since the state is restricted to the axial HF state as in Ref. [4], the corresponding energy was called *Peierls-Yoccoz rotational energy* in Ref. [23].

Equation (1) is the basic formula of the AMP. We here omit the index  $M (= 0)$  on the left-hand side (LHS) of Eq. (1). The energy difference  $\langle J|\hat{H}|J\rangle - \langle 0|\hat{H}|0\rangle$ , where  $\hat{H}$  is the Hamiltonian, is the pure rotational energy.

It has been pointed out in Ref. [23] that the cumulant expansion can straightforwardly be applied to the right-hand side (RHS) of Eq. (1). We expand  $d_{00}^{(J)}(\beta)$  by the power series of  $\beta$ ,

$$d_{00}^{(J)}(\beta) = \sum_{n=0}^{\infty} c_{2n} \beta^{2n}; \quad c_{2n} = \frac{(-)^n}{(2n)!} \langle J0|\hat{J}_y^{2n}|J0\rangle. \quad (2)$$

Note  $c_0 = 1$ ,  $c_2 = -J(J+1)/(2!2)$  and  $c_{2n} = \mathcal{O}(J^{2n})$ . The function  $\mathcal{S}^{01}(\beta)$  is defined and also expanded by the power series of  $\beta$  as follows:

$$\mathcal{S}^{01}(\beta) := \frac{\langle \Phi_0|\hat{\mathcal{S}} e^{-i\hat{J}_y\beta}|\Phi_0\rangle}{\langle \Phi_0|e^{-i\hat{J}_y\beta}|\Phi_0\rangle} = \sum_{n=0}^{\infty} s_{2n} \beta^{2n}; \quad s_{2n} = \frac{(-)^n}{(2n)!} \langle \Phi_0|\hat{\mathcal{S}}; \underbrace{\hat{J}_y; \dots; \hat{J}_y}_{2n}|\Phi_0\rangle_{\text{cum}}, \quad (3)$$

with the cumulant defined for a set of commutable operators  $\{\hat{X}_i; i = 1, 2, \dots, n\}$  [42],

$$\langle \hat{X}_1; \dots; \hat{X}_n \rangle_{\text{cum}} := \frac{\partial}{\partial t_1} \cdots \frac{\partial}{\partial t_n} \ln \left\langle \exp \left( \sum_{i=1}^n t_i \hat{X}_i \right) \right\rangle \Big|_{t_1=\dots=t_n=0}. \quad (4)$$

The low-order cumulants are represented as

$$s_0 = \langle \Phi_0|\hat{\mathcal{S}}|\Phi_0\rangle, \quad s_2 = -\frac{1}{2!} C[\hat{\mathcal{S}}, \hat{J}_y^2], \quad s_4 = \frac{1}{4!} \left( C[\hat{\mathcal{S}}, \hat{J}_y^4] - 6 C[\hat{\mathcal{S}}, \hat{J}_y^2] (\sigma[\hat{J}_y])^2 \right). \quad (5)$$

Here  $\sigma[\hat{A}]$  is the fluctuation of an operator  $\hat{A}$ , and  $C[\hat{A}, \hat{B}]$  is the correlation function of operators  $\hat{A}$  and  $\hat{B}$ ,

$$C[\hat{A}, \hat{B}] := \langle \Phi_0|\hat{A}\hat{B}|\Phi_0\rangle - \langle \Phi_0|\hat{A}|\Phi_0\rangle \langle \Phi_0|\hat{B}|\Phi_0\rangle, \quad \sigma[\hat{A}] := \sqrt{C[\hat{A}, \hat{A}]}. \quad (6)$$

Then Eq. (1) is exactly expressed in terms of the cumulants,

$$\langle J|\hat{\mathcal{S}}|J\rangle = \frac{\sum_{m,n=0}^{\infty} c_{2m} s_{2n} \Lambda_{2m+2n}}{\sum_{\ell=0}^{\infty} c_{2\ell} \Lambda_{2\ell}}, \quad (7)$$

where

$$N_{2n} := \int_0^{\pi/2} d\beta \sin \beta \beta^{2n} \langle \Phi_0|e^{-i\hat{J}_y\beta}|\Phi_0\rangle, \quad \Lambda_{2n} := \frac{N_{2n}}{N_0}, \quad (n = 0, 1, 2, \dots). \quad (8)$$

Expansion of Eq. (7) with respect to  $c_{2n}$  yields the g.s. expectation value and the  $J(J+1)$  rule for  $\langle J|\hat{\mathcal{S}}|J\rangle$ ,

$$\langle J|\hat{\mathcal{S}}|J\rangle = \langle 0|\hat{\mathcal{S}}|0\rangle + \frac{J(J+1)}{2\mathcal{I}[\hat{\mathcal{S}}]} + \dots; \quad (9a)$$

$$\langle 0|\hat{\mathcal{S}}|0\rangle := \sum_{n=0}^{\infty} s_{2n} \Lambda_{2n}, \quad \frac{1}{\mathcal{I}[\hat{\mathcal{S}}]} := \sum_{n=1}^{\infty} s_{2n} \left[ -\frac{1}{2}(\Lambda_{2n+2} - \Lambda_{2n}\Lambda_2) \right]. \quad (9b)$$

The MoI of Peierls and Yoccoz [4, 7] is obtained by neglecting the  $s_{2n}$  terms with  $n \geq 2$  for  $\hat{\mathcal{S}} = \hat{H}$ . We shall call the approximation of Eq. (9) up to the  $s_2$  terms *Peierls-Yoccoz (PY) formula*. It has been shown that the higher-order terms are not negligible in light nuclei or weakly-deformed intrinsic states [23].

The cumulant of Eq. (4) can be generalized as

$$\langle \hat{X}_1; \dots; \hat{X}_n \rangle_{\text{cum}} := \frac{\partial}{\partial t_1} \dots \frac{\partial}{\partial t_n} \ln \left\langle \prod_{i=1}^n \exp(t_i \hat{X}_i) \right\rangle \Big|_{t_1=\dots=t_n=0}, \quad (10)$$

which distinguishes the ordering of the operators on the lhs and therefore is applicable even when the operators  $\{\hat{X}_i; i = 1, 2, \dots, n\}$  are not commutable one another. The expansion is then extended to triaxially-deformed intrinsic states.

## B. Effective Hamiltonian

The nuclear effective Hamiltonian has translational, rotational, parity, and time-reversal symmetries, with the Galilean invariance and the number conservation. We assume that the individual terms of the Hamiltonian also have isospin symmetries except for the Coulomb force. The Hamiltonian is composed of the kinetic energy  $\hat{K} = \sum_i \mathbf{p}_i^2/(2M)$ , the effective nucleonic interaction  $\hat{V}_{\text{nucl}} = \sum_{i<j} \hat{v}_{ij}$ , the Coulomb interaction between protons  $\hat{V}_{\text{Coul}}$ , and the center-of-mass term  $\hat{H}_{\text{c.m.}} = \mathbf{P}^2/(2AM)$  with the total momentum  $\mathbf{P} = \sum_i \mathbf{p}_i$  and the mass number  $A = Z + N$ ,

$$\hat{H} = \hat{K} + \hat{V}_{\text{nucl}} + \hat{V}_{\text{Coul}} - \hat{H}_{\text{c.m.}}. \quad (11)$$

The effective nucleonic interaction for the self-consistent MF calculations consists of the following terms [28, 43]:

$$\hat{V}_{\text{nucl}} = \hat{V}^{(\text{C})} + \hat{V}^{(\text{LS})} + \hat{V}^{(\text{TN})} + \hat{V}^{(\text{C}\rho)}; \quad \hat{V}^{(\text{X})} = \sum_{i<j} \hat{v}_{ij}^{(\text{X})}, \quad (\text{X} = \text{C}, \text{LS}, \text{TN}, \text{C}\rho), \quad (12)$$

where  $\hat{V}^{(C)}$ ,  $\hat{V}^{(LS)}$  and  $\hat{V}^{(TN)}$  are the central, LS and tensor forces. For the individual terms of Eq. (12), we consider the following forms:

$$\begin{aligned}
\hat{v}_{ij}^{(C)} &= \sum_n (t_n^{(SE)} P_{SE} + t_n^{(TE)} P_{TE} + t_n^{(SO)} P_{SO} + t_n^{(TO)} P_{TO}) f_n^{(C)}(r_{ij}), \\
\hat{v}_{ij}^{(LS)} &= \sum_n (t_n^{(LSE)} P_{TE} + t_n^{(LSO)} P_{TO}) f_n^{(LS)}(r_{ij}) \mathbf{L}_{ij} \cdot (\mathbf{s}_i + \mathbf{s}_j), \\
\hat{v}_{ij}^{(TN)} &= \sum_n (t_n^{(TNE)} P_{TE} + t_n^{(TNO)} P_{TO}) f_n^{(TN)}(r_{ij}) r_{ij}^2 S_{ij}, \\
\hat{v}_{ij}^{(C\rho)} &= \left( t_\rho^{(SE)} P_{SE} \cdot [\rho(\mathbf{r}_i)]^{\alpha^{(SE)}} + t_\rho^{(TE)} P_{TE} \cdot [\rho(\mathbf{r}_i)]^{\alpha^{(TE)}} \right) \delta(\mathbf{r}_{ij}),
\end{aligned} \tag{13}$$

where  $\mathbf{r}_{ij} := \mathbf{r}_i - \mathbf{r}_j$ ,  $r_{ij} := |\mathbf{r}_{ij}|$ ,  $\hat{\mathbf{r}}_{ij} := \mathbf{r}_{ij}/r_{ij}$ ,  $\mathbf{p}_{ij} := (\mathbf{p}_i - \mathbf{p}_j)/2$ ,  $\mathbf{L}_{ij} := \mathbf{r}_{ij} \times \mathbf{p}_{ij}$ ,  $S_{ij} := 4[3(\mathbf{s}_i \cdot \hat{\mathbf{r}}_{ij})(\mathbf{s}_j \cdot \hat{\mathbf{r}}_{ij}) - \mathbf{s}_i \cdot \mathbf{s}_j]$ , and  $\rho(\mathbf{r})$  is the nucleon density. The central density-dependent term is distinguished from  $\hat{V}^{(C)}$  and represented by  $\hat{V}^{(C\rho)}$ . The projection operators on the singlet-even (SE), triplet-even (TE), singlet-odd (SO) and triplet-odd (TO) two-nucleon states are denoted by  $P_Y$  ( $Y = SE, TE, SO, TO$ ).

We adopt the semi-realistic interaction M3Y-P6 [29, 30, 37, 38], in which the Yukawa function  $f_n^{(X)}(r) = e^{-\mu_n^{(X)}r}/(\mu_n^{(X)}r)$  is used for the radial functions, except for  $\hat{v}_{ij}^{(C\rho)}$ . The longest-range term in  $\hat{v}_{ij}^{(C)}$  is fixed to be that of the one-pion exchange potential (OPEP). This central OPEP, denoted by  $\hat{V}^{(OPEP)}$ , is an example of spin-dependent interactions. The values of the parameters for M3Y-P6 are given in Ref. [29].

### C. MF calculations

The self-consistent MF calculations have been implemented via the Gaussian expansion method (GEM) [29, 30, 37, 38, 44]. The generalized Bogoliubov transformation in the HFB theory is given as [3, 45]

$$\alpha_i^\dagger := \sum_k \left( c_k^\dagger \mathbf{U}_{ki} + c_k \mathbf{V}_{ki} \right). \tag{14}$$

We assume the axial, time-reversal, and parity symmetry on the MF state  $|\Phi_0\rangle$ , and then the variational parameters  $\mathbf{U}_{ki}$  and  $\mathbf{V}_{ki}$  are taken to be real numbers. Adding the terms constraining the particle numbers, we modify the Hamiltonian as

$$\hat{H}' := \hat{H} - \mu_p(\hat{N}_p - Z) - \mu_n(\hat{N}_n - N), \tag{15}$$

where  $\mu_p$  ( $\mu_n$ ) is the chemical potential for protons (neutrons), and  $\hat{N}_p$  ( $\hat{N}_n$ ) is the proton (neutron) number operator. The energy  $\langle \Phi_0 | \hat{H}' | \Phi_0 \rangle$  is minimized in the HFB calculations.

We do not consider the proton-neutron pairing in this paper.

The HFB handles the pairing effects self-consistently by taking into account the influences of the pairing on the particle-hole channel. However, in the HFB, the pairing may influence the particle-hole channel and alter the HF configuration. For clarifying the effects of the pairing, the HF+BCS (Bardeen-Cooper-Schrieffer) method is useful as well, in which the HF configuration is fixed. For analyzing the pairing effects on the pure rotational energy, we introduce a parameter  $g$  as

$$\langle \hat{H}_g \rangle = \langle \hat{H}_{\text{dns}} \rangle + g \langle \hat{H}_{\text{pair}} \rangle, \quad (16)$$

where  $\langle \hat{H}_{\text{dns}} \rangle$  consists of the terms including only the density matrix, while  $\langle \hat{H}_{\text{pair}} \rangle$  is the pair energy containing the pairing tensor [3]. In the HF+BCS calculations, the axial-HF solution has been solved self-consistently, and the BCS equation is solved for  $\langle \hat{H}_g \rangle$  on top of the HF single-particle (s.p.) states. We denote its solution by  $|\Phi_0\rangle_g$ . The state  $|\Phi_0\rangle_{g=0}$  corresponds to the HF state, and the state  $|\Phi_0\rangle_{g=1}$  does to the HF+BCS state with the original Hamiltonian  $\hat{H}'$ . Throughout this paper, the parameter  $g$  is employed only in the HF+BCS scheme. We always apply  $\hat{H}'$  of Eq. (15) to the HFB calculation, not using  $\langle \hat{H}_g \rangle$ .

#### D. Implementation of AMP

In this work, the PAV has been applied for the AMP calculations of Eq. (1). The number projection is not applied. In reality, the intrinsic state could gradually change with increasing  $J$ , often accompanied by a breakdown of the axial and the time-reversal symmetry. While these effects can be handled in the cranking model [3, 6, 10] and in the VAP approaches [3], they are ignored in the present study, and we focus on the pure rotational energy, *i.e.*, the rotational energy arising from a fixed intrinsic state, as stated in Introduction.

The overlap function  $\langle \Phi_0 | e^{-i\hat{J}_y\beta} | \Phi_0 \rangle$  has been calculated from the Onishi formula [3, 9, 11, 23]. Concerning the sign problem of the Onishi formula, solutions have been proposed [46, 47] and the non-negativity of the overlap function has been proven for the HF states under the time-reversal symmetry in Appendix C of Ref. [23]. We have here confirmed via the continuity with respect to  $\beta$  that the sign of the overlap function is positive in all the cases under consideration.

There is a problem in the density-dependent coefficients in  $\hat{v}_{ij}^{(C\rho)}$  in the AMP calcula-



tions [19, 21–23]. In the present calculations, the standard treatment in Refs. [16, 23] has been adopted, replacing the density  $\rho(\mathbf{r})$  in Eq. (13) with the “*generalized density*”  $\bar{\rho}(\mathbf{r}; \beta)$ ,

$$\bar{\rho}(\mathbf{r}; \beta) := \sum_{\tau} \sum_{\sigma} \frac{\langle \Phi_0 | \hat{\rho}(\mathbf{r}\sigma\tau) e^{-i\hat{J}_y\beta} | \Phi_0 \rangle}{\langle \Phi_0 | e^{-i\hat{J}_y\beta} | \Phi_0 \rangle}; \quad \hat{\rho}(\mathbf{r}\sigma\tau) := \psi^{\dagger}(\mathbf{r}\sigma\tau)\psi(\mathbf{r}\sigma\tau), \quad (17)$$

where  $\psi^{\dagger}(\mathbf{r}\sigma\tau)$  and  $\psi(\mathbf{r}\sigma\tau)$  stand for the creation and annihilation operators for the spinor field [48], which satisfy the fermionic anticommutation relations:

$$\{\psi(x_1), \psi^{\dagger}(x_2)\} = \delta(x_1 - x_2), \quad \{\psi(x_1), \psi(x_2)\} = \{\psi^{\dagger}(x_1), \psi^{\dagger}(x_2)\} = 0. \quad (18)$$

with the shorthand notation  $x_i = (\mathbf{r}_i\sigma_i\tau_i)$  ( $i = 1, 2$ ) and  $\delta(x_1 - x_2) := \delta(\mathbf{r}_1 - \mathbf{r}_2)\delta_{\sigma_1\sigma_2}\delta_{\tau_1\tau_2}$ . Although  $\bar{\rho}(\mathbf{r}; \beta)$  in Eq. (17) is a real number, owing to the time-reversal symmetry,  $\bar{\rho}^{\alpha}(\mathbf{r}; \beta)$  is multivalued unless the power  $\alpha$  is an integer. In the M3Y-P6 interaction,  $\alpha^{(\text{SE})} = 1$  and  $\alpha^{(\text{TE})} = 1/3$  [29]. The phase of  $\bar{\rho}^{\alpha^{(\text{TE})}}(\mathbf{r}; \beta)$  has been chosen to be negative when  $\bar{\rho}(\mathbf{r}; \beta)$  is negative [23].

### E. Degree of proximity between nucleons

To investigate the relevance of the spatial correlations between nucleons to the rotational energy, we consider an operator comprised of the two-body delta function,

$$\hat{D} := \sum_{i < j} \delta(\mathbf{r}_{ij}). \quad (19)$$

The expectation value  $\langle \hat{D} \rangle$  measures the degree how frequently two constituent nucleons sit at an equal position, representing the degree that two nucleons get spatially close to each other. We call  $\langle \hat{D} \rangle$  *degree of proximity (DoP)* in this paper.

The pair-distribution function has been employed to investigate the spatial correlation between two particles [49], such as the di-neutron correlation [39]. The pair-distribution function is defined as

$$\mathcal{G}(x_1, x_2) := \frac{\langle \psi^{\dagger}(x_1)\psi^{\dagger}(x_2)\psi(x_2)\psi(x_1) \rangle}{\langle \hat{\rho}(x_1) \rangle \langle \hat{\rho}(x_2) \rangle}, \quad (20)$$

with  $x_i = (\mathbf{r}_i\sigma_i\tau_i)$ . Notice  $\mathcal{G}(x_1, x_2) = 0$  for  $x_1 = x_2$ , and  $\mathcal{G}(x_1, x_2) \geq 0$ . The DoP is regarded as a summation of the pair-distribution function at the same position, *i.e.*,

$$\begin{aligned} \langle \hat{D} \rangle &= \frac{1}{2} \sum_{\tau_1\tau_2} \sum_{\sigma_1\sigma_2} \int d^3r \langle \psi^{\dagger}(\mathbf{r}\sigma_1\tau_1)\psi^{\dagger}(\mathbf{r}\sigma_2\tau_2)\psi(\mathbf{r}\sigma_2\tau_2)\psi(\mathbf{r}\sigma_1\tau_1) \rangle \\ &= \frac{1}{2} \sum_{\tau_1\tau_2} \sum_{\sigma_1\sigma_2} \int d^3r \langle \hat{\rho}(\mathbf{r}\sigma_1\tau_1) \rangle \langle \hat{\rho}(\mathbf{r}\sigma_2\tau_2) \rangle \mathcal{G}(\mathbf{r}\sigma_1\tau_1, \mathbf{r}\sigma_2\tau_2). \end{aligned} \quad (21)$$

Since  $\hat{D}$  is a rotational scalar, the DoP for angular-momentum eigenstates  $\langle J|\hat{D}|J\rangle$  is calculable via Eq. (1). By applying  $\hat{D}P_Y$  ( $Y = \text{SE}, \text{TE}$ ) instead of  $\hat{D}$  itself, the DoP can be separated between the SE and TE channels. Restricting  $i$  and  $j$  on the RHS of Eq. (19), we can calculate the DoP for individual isospin components.

### III. RESULTS

In the present work, the AMP of Eq. (1) is implemented on top of the axial MF solutions for deformed  $_{12}\text{Mg}$  [30, 37] and  $_{40}\text{Zr}$  [38] nuclei, including stable and unstable ones. It has been established, *e.g.*, from the ratios of excitation energies  $E_x(4^+)/E_x(2^+)$  [2, 50–52], that  $^{24}_{12}\text{Mg}$ ,  $^{34-38}_{12}\text{Mg}$  [50],  $^{80}_{40}\text{Zr}$  [53] and  $^{100-110}_{40}\text{Zr}$  [2, 51, 52] are well-deformed.  $^{40}_{12}\text{Mg}$  lies near the neutron dripline [54], and a deformed halo structure has been predicted [44, 55]. In the following, we shall show the AMP results on top of the HFB solutions in  $^{24,34,40}_{12}\text{Mg}$  and  $^{80,100,104}_{40}\text{Zr}$ , whereas we limit those on top of the HF+BCS results with varying  $g$  to  $^{24}_{12}\text{Mg}$  and  $^{80,100}_{40}\text{Zr}$ , which are sufficient for the present discussion.

#### A. Influence of pairing on deformation

We define the quadrupole deformation parameter  $a_{20}$  as follows [1],

$$a_{20} := \frac{q_0}{1.09A^{5/3} \text{ fm}^2}, \quad (22)$$

where  $q_0$  is the mass quadrupole moment of the MF state [37]. In Fig. 1, the dependence of the deformation parameter  $a_{20}$  on the pairing strength  $g$  in the HF+BCS solutions [see Eq. (16)] is depicted for the  $^{34}_{12}\text{Mg}$  and  $^{80,100}_{40}\text{Zr}$  nuclei. The state  $|\Phi_0\rangle_{g=0}$  corresponds with the HF state. As  $g$  grows, the pair correlations arise at the critical values, corresponding with the normal-to-superfluid phase transition. The critical  $g$  values for proton and neutron pairs are close, though not equal. While  $a_{20}$  is insensitive to  $g$  for the  $^{80,100}_{40}\text{Zr}$  nuclei,  $a_{20}$  slightly decreases as  $g$  grows for the  $^{34}_{12}\text{Mg}$  nucleus. The values of  $a_{20}$  for the HFB minima are also shown. The  $a_{20}$  values for the HF+BCS solutions are close to that of the HFB solution for the  $^{80}_{40}\text{Zr}$  nucleus, while they do not match well for the  $^{34}_{12}\text{Mg}$  and  $^{100}_{40}\text{Zr}$  nuclei, indicating influence of the pairing on the HF configurations. Whereas the  $a_{20}$  values for the HFB solutions are smaller than those for the HF solutions in  $^{34}_{12}\text{Mg}$  and  $^{100}_{40}\text{Zr}$ , the opposite

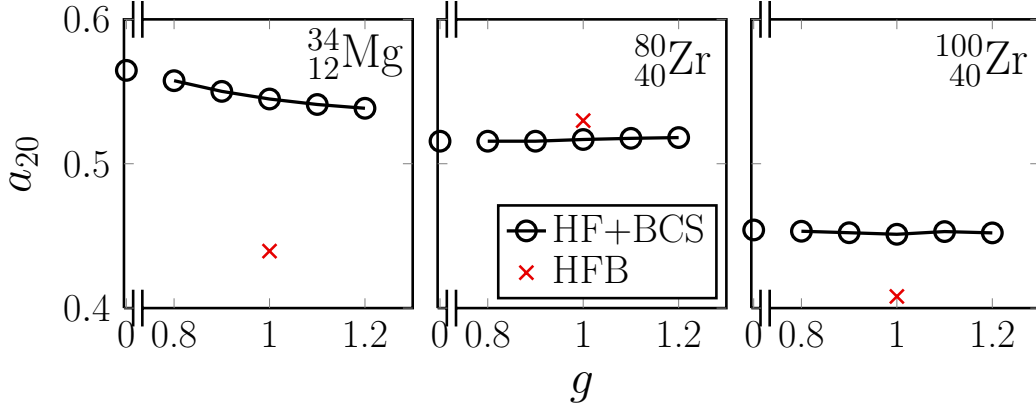


FIG. 1. The  $g$  dependence of the deformation parameter  $a_{20}$  in the HF+BCS results with  $\langle \hat{H}_g \rangle$  for  $^{34}_{12}\text{Mg}$  and  $^{80,100}_{40}\text{Zr}$ . The red crosses represent the  $a_{20}$  values in the HFB solutions.

TABLE I.  $a_{20}$  for the HF and HFB solutions at their lowest minima for  $^{24}_{12}\text{Mg}$ ,  $^{40}_{12}\text{Mg}$  and  $^{104}_{40}\text{Zr}$ .

| nuclide                | HF   | HFB  |
|------------------------|------|------|
| $^{24}_{12}\text{Mg}$  | 0.54 | 0.54 |
| $^{40}_{12}\text{Mg}$  | 0.47 | 0.43 |
| $^{104}_{40}\text{Zr}$ | 0.46 | 0.43 |

is realized at  $^{80}_{40}\text{Zr}$ . This enhancement of deformation at  $^{80}_{40}\text{Zr}$  takes place owing to the s.p. levels near the Fermi energy. The pairing moves a portion of neutrons at the highest occupied level with  $\Omega^\pi = 5/2^+$ , which originates from the  $0g_{9/2}$  spherical orbit, to the lowest unoccupied level with  $\Omega^\pi = 1/2^+$ , by which the prolate deformation is slightly enhanced. Table I presents the  $a_{20}$  values for the HF and HFB solutions at their lowest minima for  $^{24}_{12}\text{Mg}$ ,  $^{40}_{12}\text{Mg}$  and  $^{104}_{40}\text{Zr}$ .

## B. Comparison of $E_x(2^+)$ with rigid-rotor model and experiment

Let us denote the expectation value of Eq. (1) measured from that of the g.s. by

$$\mathcal{S}_x(J^+) := \langle J | \hat{\mathcal{S}} | J \rangle - \langle 0 | \hat{\mathcal{S}} | 0 \rangle. \quad (23)$$

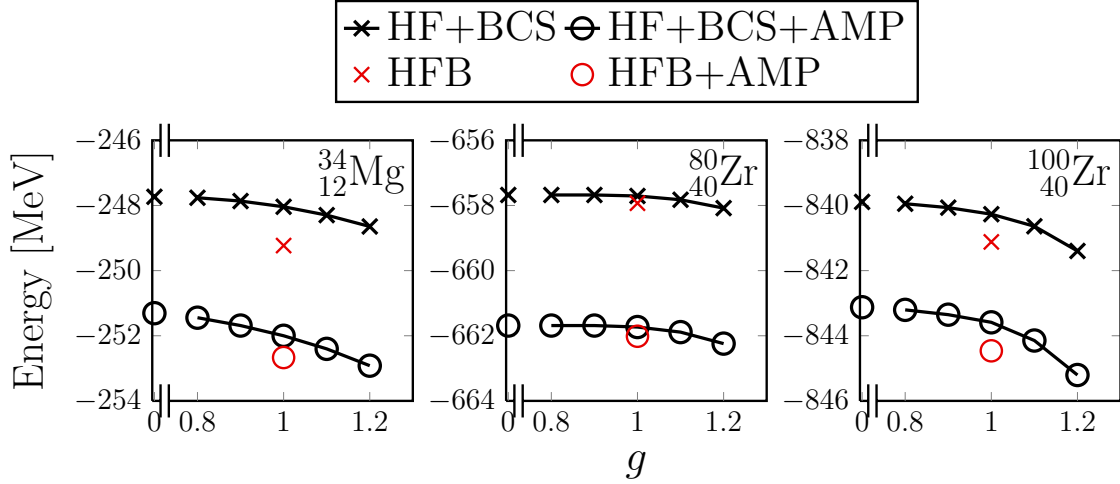


FIG. 2. The unprojected and the projected energies for  $^{34}_{12}\text{Mg}$  and  $^{80,100}_{40}\text{Zr}$ . The black crosses represent the unprojected HF+BCS energies depending on  $g$ , and the red circles do the corresponding projected energies  $E(0^+)$ . The red crosses (circles) represent the unprojected (projected) HFB energies.

We explicitly attach the parity quantum number (+) on the LHS. For  $\hat{S} = \hat{H}'$ ,  $\mathcal{S}_x(J^+)$  corresponds with the excitation energy (*i.e.*, the pure rotational energy),

$$E_x(J^+) = \langle J | \hat{H}' | J \rangle - \langle 0 | \hat{H}' | 0 \rangle. \quad (24)$$

In Fig. 2, the  $g$  dependence of the unprojected and the projected ( $E(0^+) = \langle 0 | \hat{H}' | 0 \rangle$ ) g.s. energies is shown for the HF+BCS solutions of  $^{34}_{12}\text{Mg}$  and  $^{80,100}_{40}\text{Zr}$ . Up to the critical  $g$  value where the pair correlations arise, the energies are equal to the HF case. As  $g$  increases from the critical values, both the unprojected and projected energies decrease for the HF+BCS solutions. The unprojected and projected energies for the HFB minima are also shown. Irrespective of the unprojected or the projected energies, the energies for the HFB solutions are close to those for the HF+BCS ones in the region between  $g = 1.1$  and  $1.2$ .

As it is equal to  $J(J+1)/6$  in the rigid-rotor model, the ratio  $E_x(J^+)/E_x(2^+)$  can be a measure of how well the rotational band develops. The  $g$  dependence of  $E_x(J^+)/E_x(2^+)$  is shown for the  $^{34}_{12}\text{Mg}$  and  $^{80,100}_{40}\text{Zr}$  nuclei in Fig. 3. The ratios  $E_x(J^+)/E_x(2^+)$  are insensitive to  $g$  and close to the  $J(J+1)/6$  lines except for high  $J$  ( $\gtrsim 10$ ) at  $^{34}_{12}\text{Mg}$ . For the  $^{34}_{12}\text{Mg}$  nucleus, the ratios  $E_x(J^+)/E_x(2^+)$  decrease for high  $J$  as  $g$  increases. The deviation from the  $J(J+1)/6$  lines indicates that the higher- $c_{2n}$  terms are not negligible in Eq. (7).

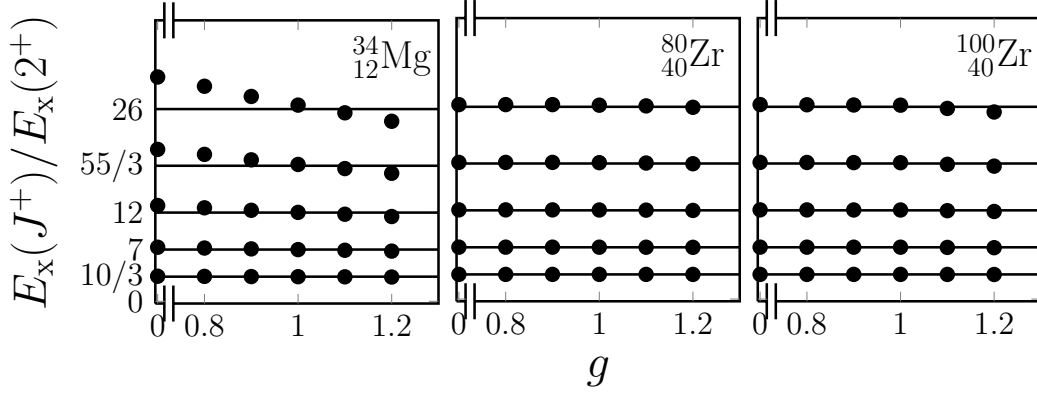


FIG. 3.  $E_x(J^+)/E_x(2^+)$  for the HF+BCS solutions of  $^{34}_{12}\text{Mg}$  and  $^{80,100}_{40}\text{Zr}$ . The lines display the rigid-rotor values  $J(J+1)/6$ .

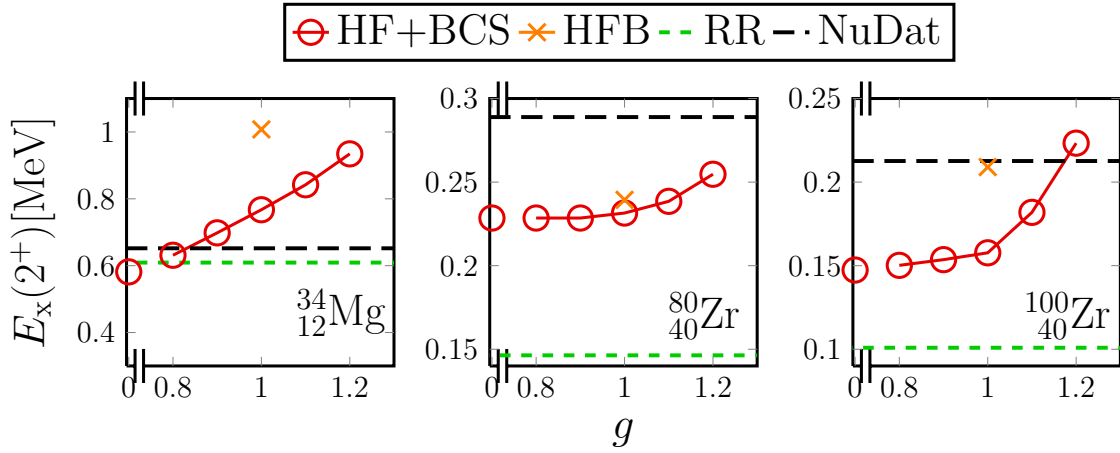


FIG. 4.  $E_x(2^+)$  for the HF+BCS solutions of  $^{34}_{12}\text{Mg}$  and  $^{80,100}_{40}\text{Zr}$ , which is represented by the red circles. The orange crosses represent the values for the HFB solutions. The black dashed lines display the experimental values [2], and the green dashed lines are the rigid-rotor values in Eq. (25) [1].

Figure 4 shows the  $g$  dependence of the excitation energies  $E_x(2^+)$  for the HF+BCS solutions of  $^{34}_{12}\text{Mg}$  and  $^{80,100}_{40}\text{Zr}$ . Those for the HFB solutions are also shown. As  $g$  increases,  $E_x(2^+)$  gets higher; the pair correlations reduce the MoI. The excitation energies  $E_x(2^+)$  of the HF+BCS solutions between  $g = 1.0$  and  $1.2$  are close to those of the HFB solutions. The  $E_x(2^+)$  values for the HFB solutions in these nuclei are about 1.5–2 times higher than

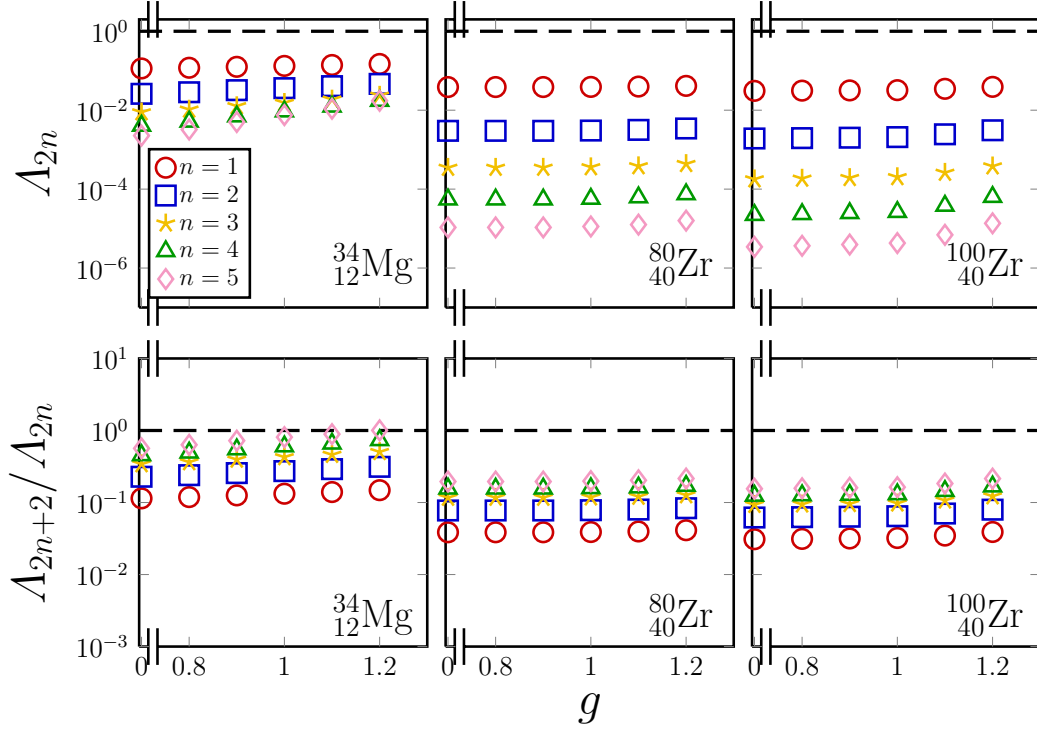


FIG. 5.  $\Lambda_{2n}$  and  $\Lambda_{2n+2}/\Lambda_{2n}$  in Eq. (8) for the HF+BCS results of  $^{34}_{12}\text{Mg}$  and  $^{80,100}_{40}\text{Zr}$ . The symbols correspond with the  $n$  values indicated in the inset.

the rigid-rotor value [1],

$$E_{\text{x}}^{(\text{RR})}(J^+) = \frac{J(J+1)}{2\mathcal{I}^{(\text{RR})}}; \quad \mathcal{I}^{(\text{RR})} \approx 0.0138 A^{5/3} [\text{MeV}^{-1}]. \quad (25)$$

Compared to the experimental values, the  $E_{\text{x}}(2^+)$  value is high in the HFB solution of the  $^{34}_{12}\text{Mg}$  nucleus, while slightly low in  $^{80,100}_{40}\text{Zr}$ .

### C. Influence of higher-order terms in cumulant expansion

We next investigate pairing effects on higher-order terms in Eq. (7). In Fig. 5, the  $g$  dependence of  $\Lambda_{2n}$  and  $\Lambda_{2n+2}/\Lambda_{2n}$  in Eq. (8) is shown for the HF+BCS solutions of  $^{34}_{12}\text{Mg}$  and  $^{80,100}_{40}\text{Zr}$ . If  $\Lambda_{2n+2}/\Lambda_{2n}$  stays small, both the  $J(J+1)$  rule and the PY approximation are validated. For growing  $g$ ,  $\Lambda_{2n}$  and  $\Lambda_{2n+2}/\Lambda_{2n}$  slightly increase for fixed  $n$ .

The g.s. correlation is defined and expanded by  $s_{2n}$  for  $\hat{\mathcal{S}} = \hat{H}'$  as

$$\Delta E_{\text{g.s.c.}} := \langle \Phi_0 | \hat{H}' | \Phi_0 \rangle - \langle 0 | \hat{H}' | 0 \rangle = - \sum_{n=1}^{\infty} s_{2n} \Lambda_{2n}. \quad (26)$$

To view the influence of the higher-order terms, we have calculated the following quantities:

$$\varepsilon_{\text{g.s.c.}}^{(k)} := \frac{-\sum_{n=1}^k s_{2n} \Lambda_{2n} - \Delta E_{\text{g.s.c.}}}{\Delta E_{\text{g.s.c.}}}, \quad (27a)$$

$$\varepsilon_{\text{x}}^{(k)} := \frac{3 \sum_{n=1}^k s_{2n} \left[ -\frac{1}{2} (\Lambda_{2n+2} - \Lambda_{2n} \Lambda_2) \right] - E_{\text{x}}(2^+)}{E_{\text{x}}(2^+)}. \quad (27b)$$

We calculate  $s_2$  and  $s_4$  from Eq. (3) via numerical differentiation. The values of  $\varepsilon_{\text{g.s.c.}}^{(k)}$  and  $\varepsilon_{\text{x}}^{(k)}$  ( $k = 1, 2$ ) are shown for  $^{34}_{12}\text{Mg}$  and  $^{80,100}_{40}\text{Zr}$  in Fig. 6. Insensitive to  $g$ ,  $\varepsilon_{\text{g.s.c.}}^{(1)}$  and  $\varepsilon_{\text{x}}^{(1)}$  almost vanish for  $^{80,100}_{40}\text{Zr}$ . Namely, the contributions of the higher- $s_{2n}$  terms to  $\Delta E_{\text{g.s.c.}}$  and  $E_{\text{x}}(2^+)$  are negligible, and the PY formula (Eq. (9b) truncated at  $n = 1$ ) is good. On the other hand, the  $\varepsilon_{\text{g.s.c.}}^{(1)}$  and  $\varepsilon_{\text{x}}^{(1)}$  values become larger as  $g$  increases in the  $^{34}_{12}\text{Mg}$  nucleus. The pair correlations enhance the higher- $s_{2n}$  terms of the cumulant expansion, the terms including  $s_4$  in practice, in the g.s. correlations and the MoI of this light nucleus. The  $\varepsilon_{\text{g.s.c.}}^{(2)}$  and  $\varepsilon_{\text{x}}^{(2)}$  values are vanishing.

In Fig. 6, the values of  $\varepsilon_{\text{g.s.c.}}^{(k)}$  and  $\varepsilon_{\text{x}}^{(k)}$  for  $k = 1, 2$  are also shown for the HFB solutions of  $^{34}_{12}\text{Mg}$  and  $^{80,100}_{40}\text{Zr}$ . The results are similar to the HF+BCS cases. While the  $\varepsilon_{\text{g.s.c.}}^{(1)}$  and  $\varepsilon_{\text{x}}^{(1)}$  values are less than 10% for  $^{80,100}_{40}\text{Zr}$ , the  $s_4$  terms are sizable for the  $^{34}_{12}\text{Mg}$  nucleus. This consequence is qualitatively similar also to the HF case in Ref. [23].

#### D. Contribution of constituent terms of effective Hamiltonian

In Ref. [23], we analyzed the composition of the pure rotational energy of the axial-HF solutions. In this subsection, we present influences of the pairing on the composition of the pure rotational energy. By taking  $\hat{\mathcal{S}}$  to be constituent terms of  $\hat{H}'$ , the  $\mathcal{S}_{\text{x}}(J^+)$  values of Eq. (23) yield their contributions to the rotational energy. In the following,  $\hat{\mathcal{S}}$  is an element of the following set,

$$\hat{\mathcal{S}} \in \{\hat{H}', \hat{K}, \hat{V}^{(\text{C})}, \hat{V}^{(\text{LS})}, \hat{V}^{(\text{TN})}, \hat{V}^{(\text{C}\rho)}, \hat{V}^{(\text{OPEP})}, \hat{H}_{\text{pair}}\}. \quad (28)$$

Each element has been defined in Sec. II. Since  $\langle J | \hat{N}_p | J \rangle \neq Z$  and  $\langle J | \hat{N}_n | J \rangle \neq N$ , the chemical-potential terms in Eq. (15) have contributions to the rotational energy, which

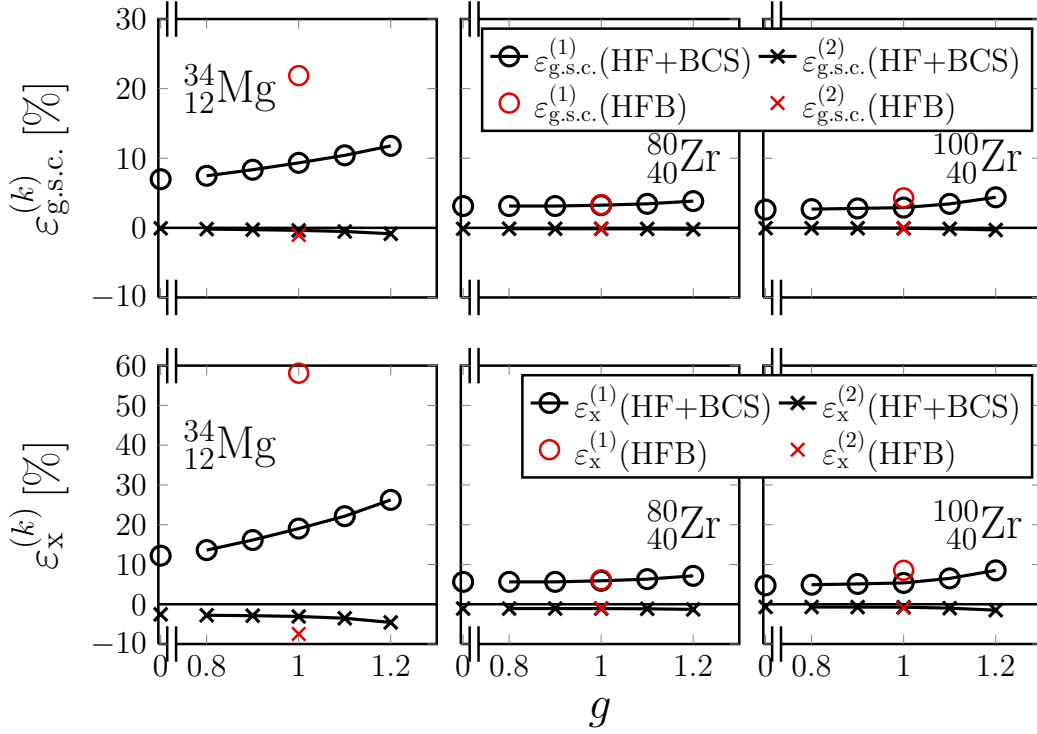


FIG. 6.  $\varepsilon_{\text{g.s.c.}}^{(k)}$  and  $\varepsilon_x^{(k)}$  ( $k = 1, 2$ ) in the HF+BCS and HFB solutions of  $^{34}_{12}\text{Mg}$  and  $^{80,100}_{40}\text{Zr}$ .

should be attributed to other terms of the Hamiltonian if the particle-number projection is simultaneously implemented. However, they are insignificant, staying within  $-0.5 - 17\%$  for the MF states under investigation.

In Fig. 7, the  $g$  dependence of  $\mathcal{S}_x(4^+)/\mathcal{S}_x(2^+)$ , the ratios given by the constituent terms of the effective Hamiltonian, is shown for the  $^{34}_{12}\text{Mg}$  and  $^{80,100}_{40}\text{Zr}$  nuclei. Contributions of the pairing tensors are excluded except for  $\hat{H}_{\text{pair}}$ . The ratios are close to  $10/3$  for  $^{80,100}_{40}\text{Zr}$ , almost independent of  $g$  and  $\hat{\mathcal{S}}$ . In  $^{34}_{12}\text{Mg}$ , the ratios  $\mathcal{S}_x(4^+)/\mathcal{S}_x(2^+)$  for  $\hat{\mathcal{S}} = \hat{K}$ ,  $\hat{V}^{(\text{TN})}$  and  $\hat{H}_{\text{pair}}$  are also almost independent of  $g$ , while those for  $\hat{V}^{(\text{C})}$ ,  $\hat{V}^{(\text{LS})}$ ,  $\hat{V}^{(\text{C}\rho)}$  and  $\hat{V}^{(\text{OPEP})}$  become deviating from  $10/3$  as  $g$  increases. The irregular behavior for  $\hat{V}^{(\text{C})}$  and  $\hat{V}^{(\text{OPEP})}$  observed at  $g \approx 1.1$  in  $^{34}_{12}\text{Mg}$  happens because  $\mathcal{S}_x(2^+) \approx 0$  in this region, with sign inversion (see Fig. 8).

As long as any  $\mathcal{S}_x(J^+)/\mathcal{S}_x(2^+)$  is close to  $J(J+1)/6$ ,  $\mathcal{S}_x(J^+)$  is well described by  $\mathcal{I}[\hat{\mathcal{S}}]$  in Eq. (9a), and it is sufficient to inspect  $\mathcal{S}_x(2^+)$  in analyzing the rotational energy. The contributions of the constituent terms of the effective Hamiltonian to the total rotational energy are represented by  $\mathcal{S}_x(2^+)/E_x(2^+)$ . In Fig. 8, the  $g$  dependence of  $\mathcal{S}_x(2^+)/E_x(2^+)$  is shown for  $^{34}_{12}\text{Mg}$  and  $^{80,100}_{40}\text{Zr}$ . As  $g$  increases from the critical points, the  $\mathcal{S}_x(2^+)/E_x(2^+)$  values for  $\hat{\mathcal{S}} = \hat{K}$ ,  $\hat{V}^{(\text{C})}$  and  $\hat{V}^{(\text{C}\rho)}$  vary; decrease for  $\hat{\mathcal{S}} = \hat{V}^{(\text{C})}$ , while increase for  $\hat{V}^{(\text{C}\rho)}$ .



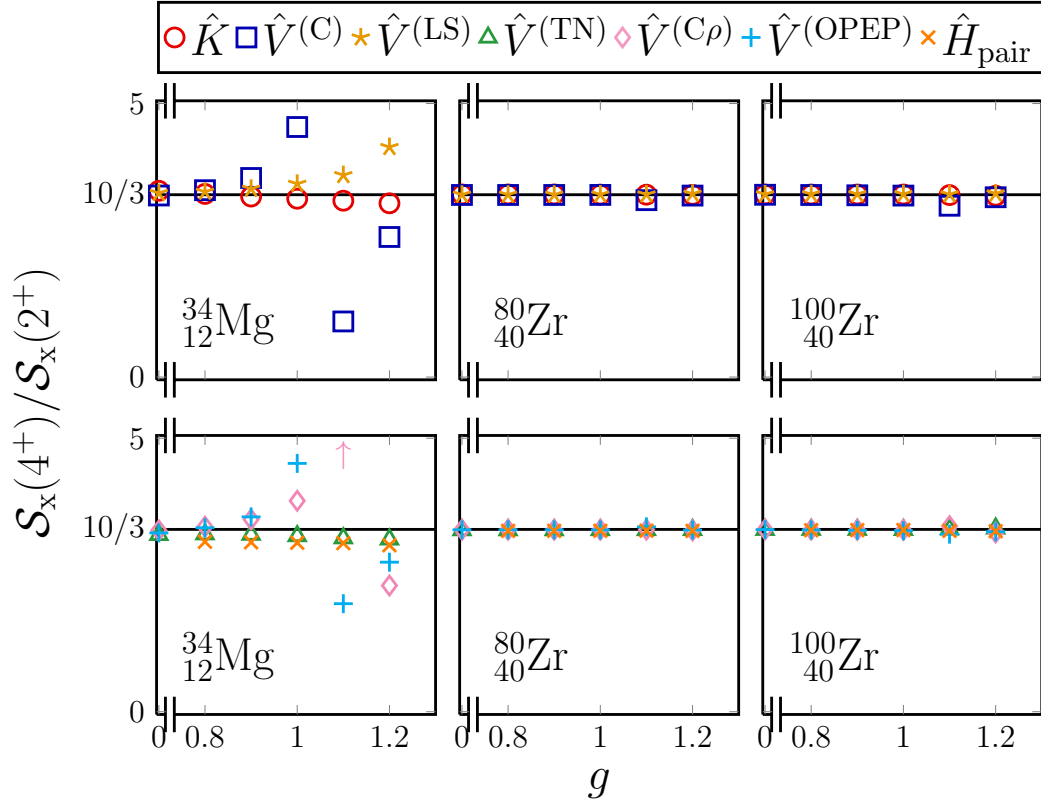


FIG. 7.  $\mathcal{S}_x(4^+)/\mathcal{S}_x(2^+)$  for  $\hat{\mathcal{S}} = \hat{K}$  (red circles),  $\hat{V}^{(C)}$  (blue squares),  $\hat{V}^{(LS)}$  (yellow stars),  $\hat{V}^{(TN)}$  (green triangles),  $\hat{V}^{(C\rho)}$  (pink diamonds) and  $\hat{V}^{(OPEP)}$  (sky-blue pluses) in the HF+BCS results of  $^{34}_{12}\text{Mg}$  and  $^{80,100}_{40}\text{Zr}$ .  $\mathcal{S}_x(4^+)/\mathcal{S}_x(2^+)$  for  $\hat{H}_{\text{pair}}$  are represented by the orange crosses. The rigid-rotor value  $10/3$  is displayed by the horizontal lines.

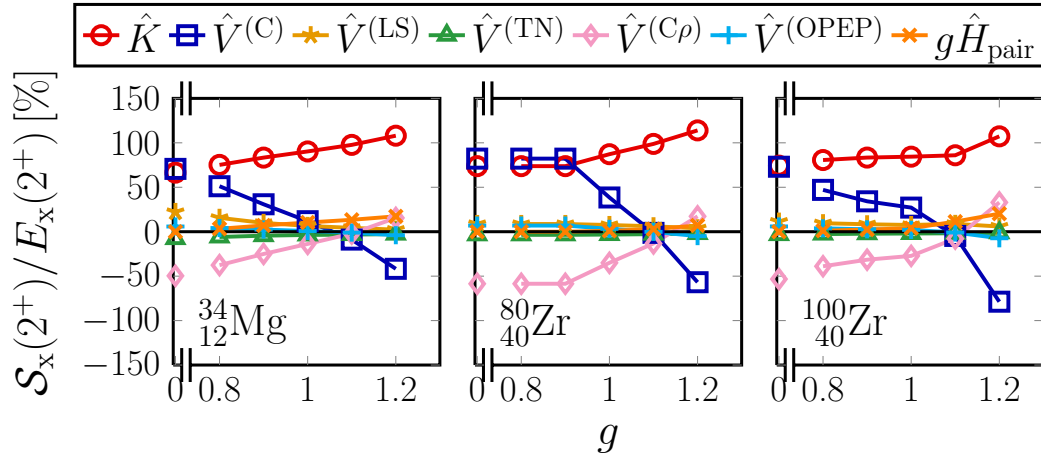


FIG. 8. The ratios  $\mathcal{S}_x(2^+)/E_x(2^+)$ . See Fig. 7 for conventions.

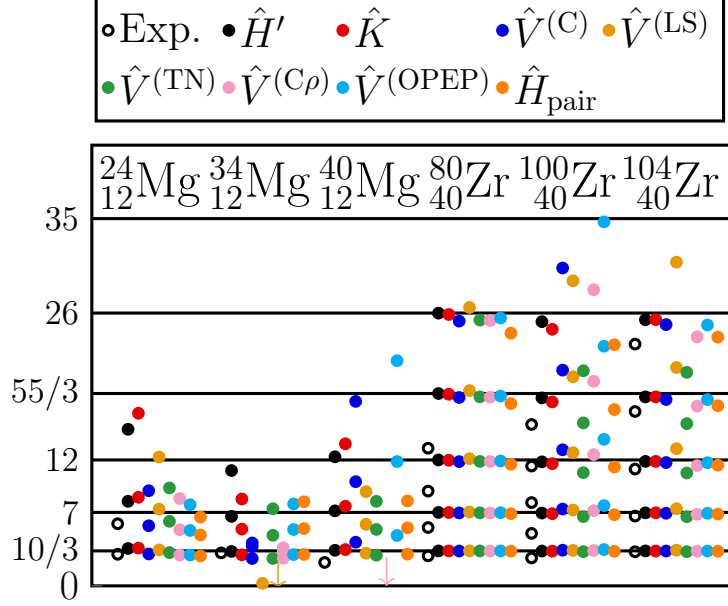


FIG. 9.  $\mathcal{S}_x(J^+)/\mathcal{S}_x(2^+)$  for the HFB solutions of the  $^{24,34,40}_{12}\text{Mg}$  and  $^{80,100,104}_{40}\text{Zr}$  nuclei. See Fig. 7 for conventions. The experimental values of  $E_x(J^+)/E_x(2^+)$  are taken from Refs. [2, 50, 56].

Even their signs are inverted near  $g = 1.1$ . As  $g$  increases, the contribution of  $g\hat{H}_{\text{pair}}$  to the rotational energy is enhanced, which is dominated by the central force. The contributions of  $\hat{V}_{\text{Coul}}$ ,  $\hat{H}_{\text{c.m.}}$  and  $\hat{V}^{(\text{OPEP})}$  to  $E_x(2^+)$  are  $\pm 10\%$  at most.

Figure 9 shows the ratios  $\mathcal{S}_x(J^+)/\mathcal{S}_x(2^+)$  for the HFB solutions of the  $^{24,34,40}_{12}\text{Mg}$  and  $^{80,100,104}_{40}\text{Zr}$  nuclei, all of which have prolate shapes. The ratios  $E_x(4^+)/E_x(2^+)$  obtained in the present work are close to those of the experiments and  $10/3$  except at  $^{40}_{12}\text{Mg}$ . For the deformed  $_{40}\text{Zr}$  nuclei, the ratios of the constituent terms  $\mathcal{S}_x(J^+)/\mathcal{S}_x(2^+)$  are also close to  $J(J+1)/6$ , although less close than in the HF case. On the other hand, some ratios  $\mathcal{S}_x(J^+)/\mathcal{S}_x(2^+)$  do not obey the  $J(J+1)$  rule for the  $_{12}\text{Mg}$  nuclei. We find several cases in which even  $\langle J|\hat{\mathcal{S}}|J \rangle$  is not monotonic for  $J$ , *e.g.*, with  $\mathcal{S}_x(4^+)/\mathcal{S}_x(2^+) < 1$ .

In Fig. 10,  $\mathcal{S}_x(2^+)/E_x(2^+)$  are shown for the HFB solutions of the  $^{24,34,40}_{12}\text{Mg}$  and  $^{80,100,104}_{40}\text{Zr}$  nuclei. The results significantly depend on the nuclei. The contribution of the kinetic energy  $\hat{\mathcal{S}} = \hat{K}$  is large. It is remarked that those of the interactions  $\hat{V}^{(\text{C})}$  and  $\hat{V}^{(\text{C}\rho)}$  are scattered, in sharp contrast to the results for the deformed HF solutions in Fig. 3 of Ref. [23]. For the HF solutions, the composition of the pure rotational energy for the well-deformed heavy nuclei is insensitive to nuclides and deformation. However, as elucidated in Fig. 8,  $\mathcal{S}_x(2^+)/E_x(2^+)$  is sensitive to the pairing. Since the degree of the pair correlations depends on nuclei, the

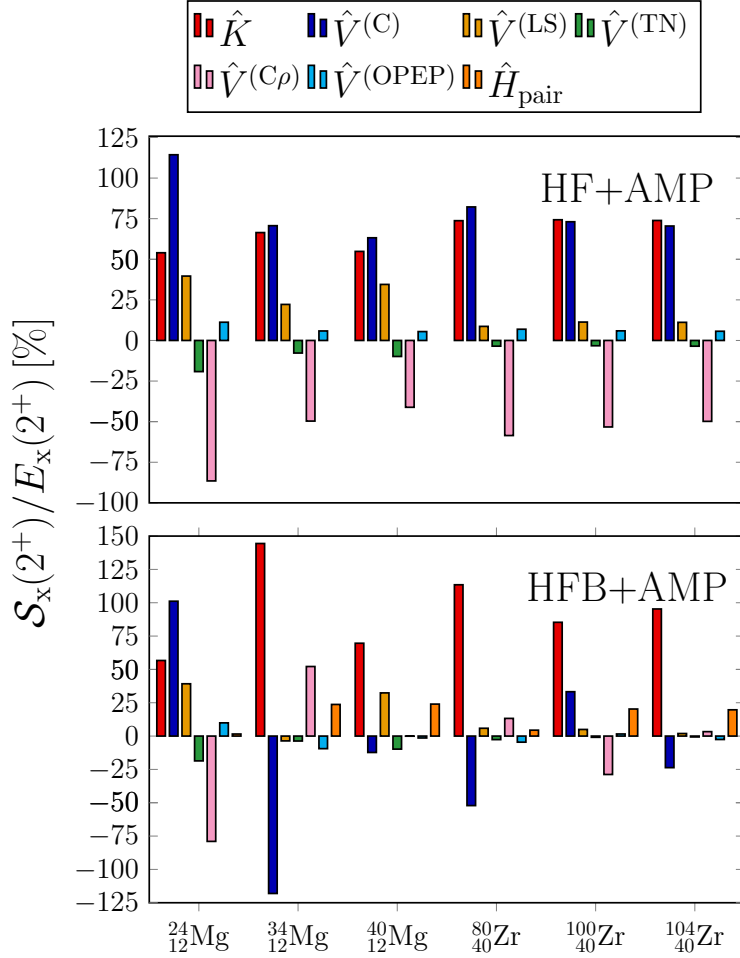


FIG. 10.  $S_x(2^+)/E_x(2^+)$  for the HFB solutions (lower panel) of the  $^{24,34,40}_{12}\text{Mg}$  and  $^{80,100,104}_{40}\text{Zr}$  nuclei, in comparison with those for the HF solutions (upper panel) [23].

components of the pure rotational energy of nuclei also do, even for the well-deformed heavy nuclei.

### E. Angle dependence of integrands of Eq. (1)

In Ref. [23], we showed that the overlap functions  $\langle \Phi_0 | e^{-i\hat{J}_y\beta} | \Phi_0 \rangle$  and  $\mathcal{S}^{01}(\beta)$  in Eq. (3) are relevant to the  $J(J+1)$  rule and the composition of the rotational energy. The dependence of the overlap functions on the angle  $\beta$  will be instructive in the HF+BCS and HFB cases, as well.

Figure 11 shows the  $g$  dependence of the overlap functions  $\langle \Phi_0 | e^{-i\hat{J}_y\beta} | \Phi_0 \rangle_g$  for the HF+BCS solutions of  $^{34}_{12}\text{Mg}$  and  $^{80,100}_{40}\text{Zr}$ . For  $^{80,100}_{40}\text{Zr}$ ,  $\langle \Phi_0 | e^{-i\hat{J}_y\beta} | \Phi_0 \rangle_g$  have sharp peaks near

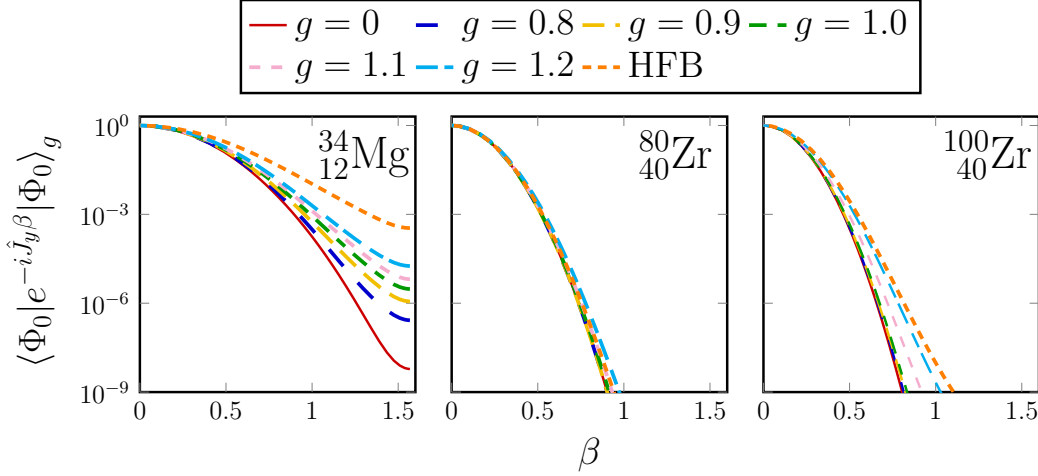


FIG. 11. The overlap functions  $\langle \Phi_0 | e^{-i\hat{J}_y\beta} | \Phi_0 \rangle_g$  in the HF+BCS and HFB solutions of  $^{34}_{12}\text{Mg}$  and  $^{80,100}_{40}\text{Zr}$ . The individual lines correspond to the  $g$  values shown in the inset.

$\beta = 0$ , and become slightly broader as  $g$  increases. In contrast,  $\langle \Phi_0 | e^{-i\hat{J}_y\beta} | \Phi_0 \rangle_g$  have broad peaks near  $\beta = 0$  and getting much broader for increasing  $g$  for the  $^{34}_{12}\text{Mg}$  nucleus.

Figure 11 also depicts  $\langle \Phi_0 | e^{-i\hat{J}_y\beta} | \Phi_0 \rangle$  for the HFB solutions of  $^{34}_{12}\text{Mg}$  and  $^{80,100}_{40}\text{Zr}$ . The overlap functions  $\langle \Phi_0 | e^{-i\hat{J}_y\beta} | \Phi_0 \rangle$  for  $^{80,100}_{40}\text{Zr}$  have sharper peaks near  $\beta = 0$  than those for  $^{34}_{12}\text{Mg}$ . The broad peak near  $\beta = 0$  makes the ratios  $\mathcal{S}_x(J^+)/\mathcal{S}_x(2^+)$  deviate from  $J(J+1)/6$  in Fig. 9, as analogous arguments given in Ref. [23]. The curvature of  $\langle \Phi_0 | e^{-i\hat{J}_y\beta} | \Phi_0 \rangle$  at  $\beta = 0$  is equal to the variance  $(\sigma[\hat{J}_y])^2$  apart from the sign (see Eq. (6)),

$$-\frac{d^2}{d\beta^2} \langle \Phi_0 | e^{-i\hat{J}_y\beta} | \Phi_0 \rangle \Big|_{\beta=0} = (\sigma[\hat{J}_y])^2. \quad (29)$$

In Fig. 12, we show  $(\sigma[\hat{J}_y])^2$  for  $^{34}_{12}\text{Mg}$  and  $^{80,100}_{40}\text{Zr}$ . Regardless of nuclei, the  $(\sigma[\hat{J}_y])^2$  values decrease as  $g$  increases, and  $(\sigma[\hat{J}_y])^2$  of the HFB solutions are smaller than that of the HF solutions. The  $^{100}_{40}\text{Zr}$  nucleus exemplifies that  $a_{20}$  does not well correlate to  $\sigma[\hat{J}_y]$  straightforwardly;  $(\sigma[\hat{J}_y])^2$  substantially decreases as  $g$  grows, while  $a_{20}$  shown in Fig. 1 is insensitive to  $g$ .

We next investigate the inversion near  $g = 1.1$  for  $\hat{\mathcal{S}} = \hat{V}^{(C)}$  and  $\hat{V}^{(C\rho)}$  observed in Fig. 8, at the level of the overlap functions. By using Eq. (3), we define  $\Delta\mathcal{S}^{01}(\beta)$  as

$$\Delta\mathcal{S}^{01}(\beta) := \mathcal{S}^{01}(\beta) - \mathcal{S}^{01}(\beta = 0). \quad (30)$$

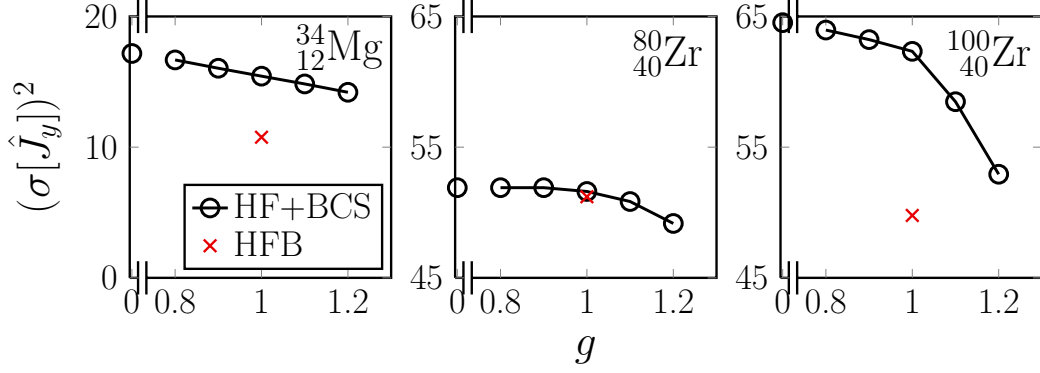


FIG. 12.  $(\sigma[\hat{J}_y])^2$  in the HF+BCS and HFB solutions of  $^{34}_{12}\text{Mg}$  and  $^{80,100}_{40}\text{Zr}$ .

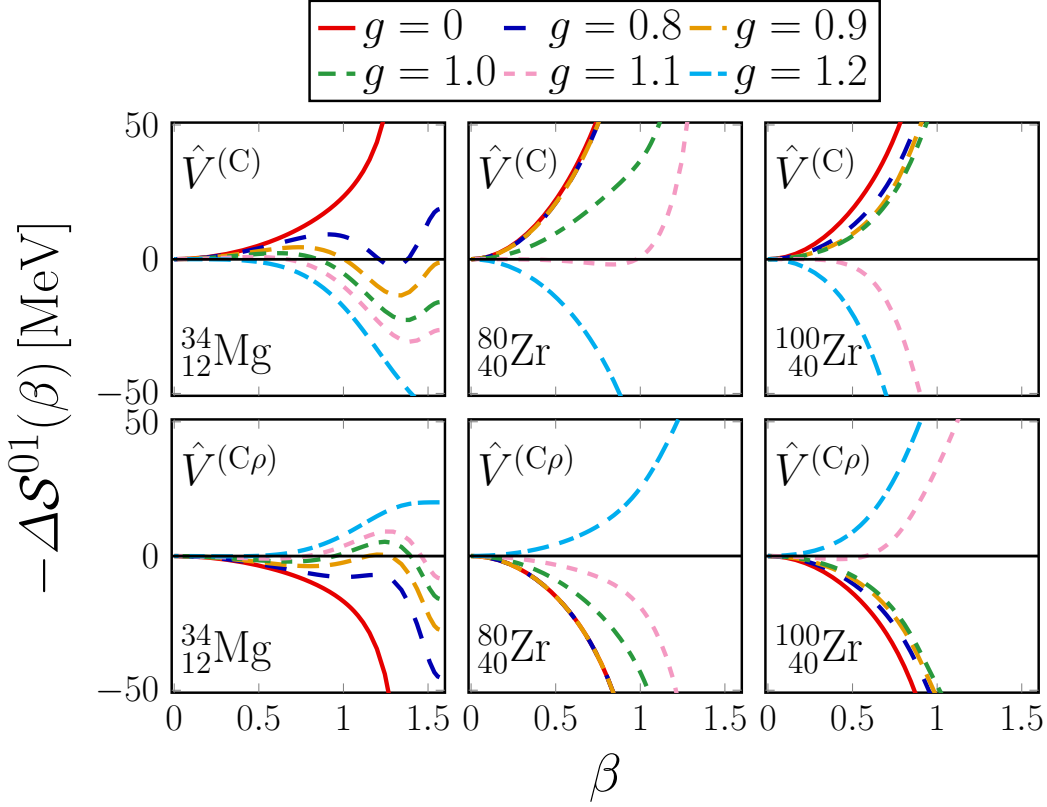


FIG. 13.  $-\Delta\mathcal{S}^{01}(\beta)$  for  $\hat{\mathcal{S}} = \hat{V}^{(C)}$  and  $\hat{V}^{(C\rho)}$  in the HF+BCS solutions of  $^{34}_{12}\text{Mg}$  and  $^{80,100}_{40}\text{Zr}$ . The individual lines correspond to the  $g$  values shown in the inset.

The curvature of  $-\Delta\mathcal{S}^{01}(\beta)$  is related to the correlation function  $C[\hat{\mathcal{S}}, \hat{J}_y^2]$ ,

$$-\frac{d^2}{d\beta^2} \Delta\mathcal{S}^{01}(\beta) \Big|_{\beta=0} = C[\hat{\mathcal{S}}, \hat{J}_y^2]. \quad (31)$$

Although this relation is not exact for  $\hat{v}_{ij}^{(C\rho)}[\bar{\rho}(\mathbf{r}_i; \beta)]$  because of the  $\beta$ -dependence of  $\bar{\rho}$ ,

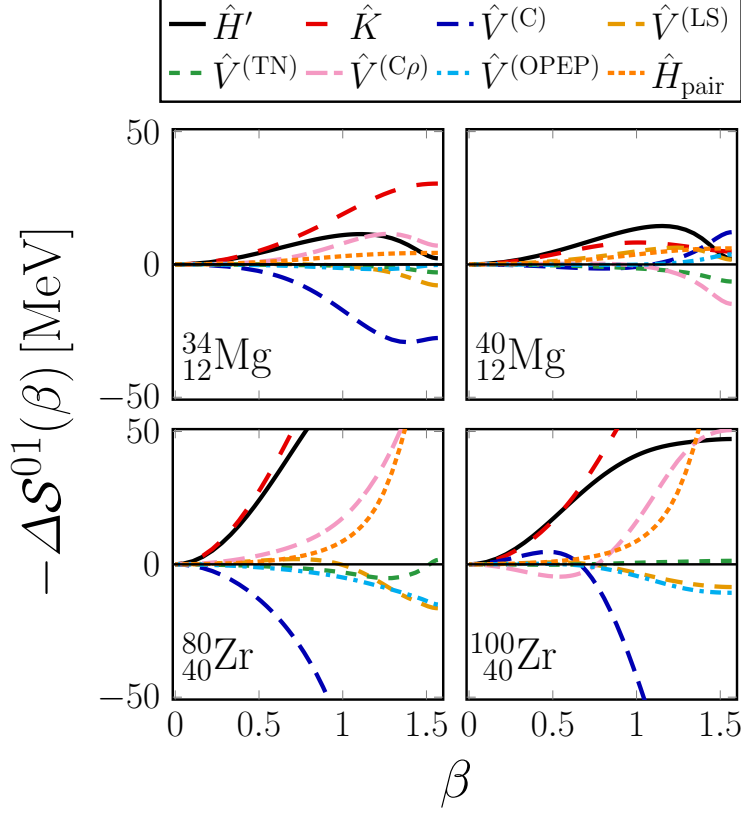


FIG. 14.  $-\Delta\mathcal{S}^{01}(\beta)$  for the constituent terms of the Hamiltonian for the HFB solutions of  $^{34,40}_{12}\text{Mg}$  and  $^{80,100}_{40}\text{Zr}$ .

Eq. (31) holds approximately. Figure 13 shows the  $g$  dependence of  $-\Delta\mathcal{S}^{01}(\beta)$  in Eq. (30) for  $\hat{\mathcal{S}} = \hat{V}^{(C)}$  and  $\hat{V}^{(C\rho)}$  in  $^{34}_{12}\text{Mg}$  and  $^{80,100}_{40}\text{Zr}$ . As  $g$  increases, the behavior of  $-\Delta\mathcal{S}^{01}(\beta)$  drastically changes. The signs of  $-\Delta\mathcal{S}^{01}(\beta)$  near  $\beta = 0$ , which is related to  $C[\hat{\mathcal{S}}, \hat{J}_y^2]$  via Eq. (31), changes from positive (negative) to negative (positive) for  $\hat{\mathcal{S}} = \hat{V}^{(C)}$  ( $\hat{V}^{(C\rho)}$ ). The results in Fig. 13 correspond to those in Fig. 8 via the MoI of Eq. (9). As a function of  $\beta$ ,  $-\Delta\mathcal{S}^{01}(\beta)$  for  $^{34}_{12}\text{Mg}$  changes more slowly than those for  $^{80,100}_{40}\text{Zr}$ . This almost flat structure of  $-\Delta\mathcal{S}^{01}(\beta)$  for  $^{34}_{12}\text{Mg}$  gives rise to the deviation from the  $J(J+1)$  rule and the irregular  $J$  ordering in Fig. 9. The results in Fig. 13 correspond well to those in Figs. 7 and 8.

In Fig. 14, we show  $-\Delta\mathcal{S}^{01}(\beta)$  for the HFB solutions of  $^{34,40}_{12}\text{Mg}$  and  $^{80,100}_{40}\text{Zr}$ . These results are relevant to those in Fig. 10. The  $|C[\hat{\mathcal{S}}, \hat{J}_y^2]|$  values (see Eq. (31)) significantly increase for  $\hat{\mathcal{S}} = \hat{K}$ ,  $\hat{V}^{(C)}$  and  $\hat{V}^{(C\rho)}$  as the mass number increases. The signs of  $C[\hat{\mathcal{S}}, \hat{J}_y^2]$  for  $\hat{H}_{\text{pair}}$  are positive without exceptions. The signs of  $C[\hat{\mathcal{S}}, \hat{J}_y^2]$  for  $\hat{\mathcal{S}} = \hat{V}^{(C)}$  are negative, and those for  $\hat{V}^{(C\rho)}$  are positive for  $^{34}_{12}\text{Mg}$  and  $^{80}_{40}\text{Zr}$ , which are opposite to the results for the HF solutions

in Fig. 13 of Ref. [23]. The pair correlations could change the signs of  $C[\hat{\mathcal{S}}, \hat{J}_y^2]$  for  $\hat{\mathcal{S}} = \hat{V}^{(C)}$  and  $\hat{V}^{(C\rho)}$ , leading to the results in Fig. 10. Even though the HFB solution of  $^{100}_{40}\text{Zr}$  has the pair correlations,  $C[\hat{\mathcal{S}}, \hat{J}_y^2]$  is positive (negative) for  $\hat{\mathcal{S}} = \hat{V}^{(C)}$  ( $\hat{V}^{(C\rho)}$ ). The flat structure of  $-\Delta\mathcal{S}^{01}(\beta)$  for  $\hat{\mathcal{S}} = \hat{V}^{(\text{LS})}$  in  $^{34}_{12}\text{Mg}$  and  $\hat{V}^{(C\rho)}$  in  $^{40}_{12}\text{Mg}$  corresponds to the deviation from  $J(J+1)/6$  and the irregular  $J$  ordering in Fig. 9. The results in Fig. 14 well account for those in Figs. 9 and 10.

### F. Degree of proximity for nucleons associated with nucleonic interaction

We have found that the pairing greatly influences the contribution of  $\hat{V}^{(C)}$  and  $\hat{V}^{(C\rho)}$  to the rotational energy. In the preceding subsection, their contributions have been analyzed in terms of  $-\Delta\mathcal{S}^{01}(\beta)$ . To investigate what governs the contributions of  $\hat{V}^{(C)}$  and  $\hat{V}^{(C\rho)}$  further, we calculate the DoP  $\langle\hat{D}\rangle$  by using the AMP, which has been defined in Sec. II E.

Denoting the increment of  $\langle\hat{D}\rangle$  by  $\Delta D$  as

$$\Delta D := \langle\Phi_0|\hat{D}|\Phi_0\rangle_g - \langle\Phi_0|\hat{D}|\Phi_0\rangle_{g=0}, \quad (32)$$

the  $g$  dependence of  $\Delta D$  is shown for the HF+BCS solutions of  $^{34}_{12}\text{Mg}$  and  $^{80,100}_{40}\text{Zr}$  in Fig. 15. The  $\langle\Phi_0|\hat{D}|\Phi_0\rangle_{g=0}$  values for  $^{34}_{12}\text{Mg}$ ,  $^{80}_{40}\text{Zr}$  and  $^{100}_{40}\text{Zr}$  are 1.22, 3.43 and 4.28, respectively. As expected,  $\Delta D$  increases for increasing  $g$ . Analogously to Eq. (16), we separate the DoP  $\langle\hat{D}\rangle$  as

$$\langle\hat{D}\rangle = \langle\hat{D}_{\text{dns}}\rangle + \langle\hat{D}_{\text{pair}}\rangle. \quad (33)$$

Owing to the locality of the operator  $\hat{D}$ ,  $\langle\hat{D}_{\text{dns}}\rangle$  consists of the SE (viz.  $T = 1$ ) and the TE (viz.  $T = 0$ ) channels, while  $\langle\hat{D}_{\text{pair}}\rangle$  has only the SE channel. The  $\Delta D$  values for the individual isospin components,  $pp$ ,  $nn$ ,  $pn$  with  $T = 1$  and 0, are also shown. For the TE channel, we take the arithmetic average of the three components of the spin-triplet. The contributions of  $\langle\Phi_0|\hat{D}_{\text{pair}}|\Phi_0\rangle_g$  to  $\Delta D$  tend to be larger than those of  $\langle\Phi_0|\hat{D}_{\text{dns}}|\Phi_0\rangle_g$ .

We have calculated  $\langle J|\hat{D}|J\rangle$ , the DoP at angular-momentum eigenstates, for the HF+BCS and HFB solutions of  $^{34}_{12}\text{Mg}$  and  $^{80,100}_{40}\text{Zr}$ . The  $g$  dependence of  $\langle J|\hat{D}|J\rangle_g - \langle J|\hat{D}|J\rangle_{g=0}$  behaves similarly to that of  $\Delta D$  in Fig. 15. We then define  $D_x(J^+)$  as

$$D_x(J^+) := \langle J|\hat{D}|J\rangle - \langle 0|\hat{D}|0\rangle, \quad (34)$$

which corresponds with Eq. (23) for  $\hat{\mathcal{S}} = \hat{D}$ . As the intrinsic state  $|\Phi_0\rangle$  is identical among  $|J\rangle$  ( $J = 0, 2, 4, \dots$ ),  $D_x(J^+)$  are small, but do not vanish. The  $g$  dependence of  $D_x(2^+)$  for

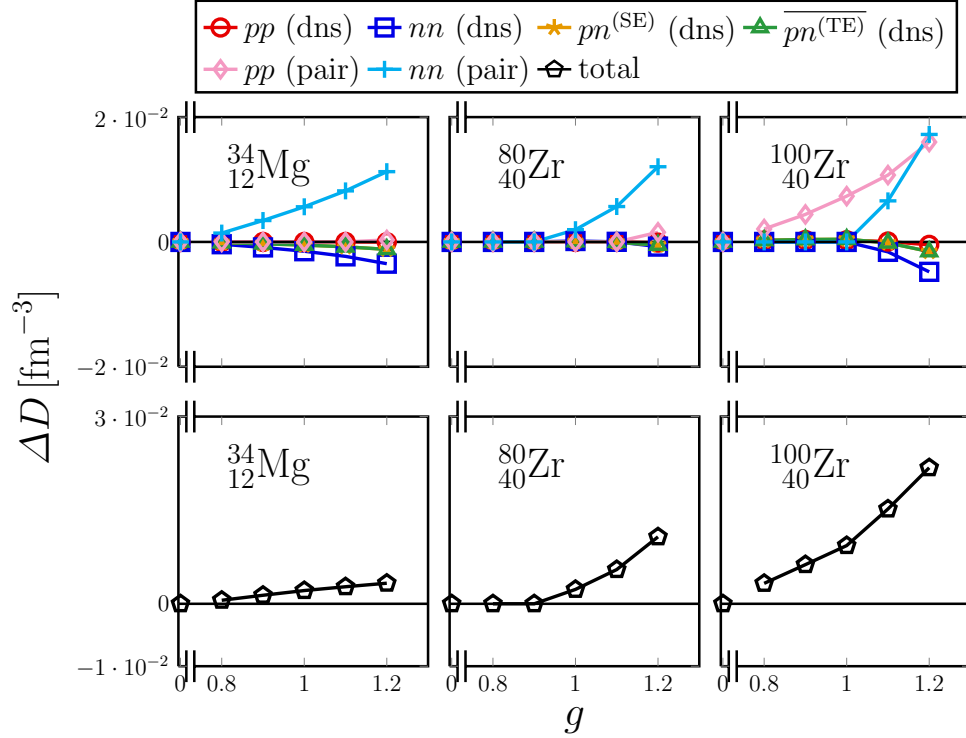


FIG. 15.  $\Delta D$  for the HF+BCS solutions of  $^{34}_{12}\text{Mg}$  and  $^{80,100}_{40}\text{Zr}$ . The black pentagons in the lower panels are the total values of  $\Delta D$ . The separated values of  $\Delta D$  into the individual isospin components are also shown; the  $pp$  (red circles),  $nn$  (blue squares), and  $pn$  correlations (yellow stars) of the SE channel in  $\langle \hat{D}_{\text{dns}} \rangle$ , where  $p$  ( $n$ ) stands for protons (neutrons). The arithmetic average of the spin components is plotted for the  $\Delta D$  values of the TE channel (green triangles). The  $pp$  and  $nn$  correlations of the pairing channel in  $\langle \hat{D}_{\text{pair}} \rangle$  in Eq. (33) are represented as pink diamonds and sky-blue pluses, respectively.

the HF+BCS solutions of  $^{34}_{12}\text{Mg}$  and  $^{80,100}_{40}\text{Zr}$  are exhibited in Fig. 16. The values of  $D_x(2^+)$  for the HFB solutions (with  $g = 1$ ) are also shown for reference. In  $^{80}_{40}\text{Zr}$ ,  $D_x(2^+)$  for the HFB solution is close to those for the HF+BCS solutions at  $g \approx 1.2$ . No  $g$  values match the HFB results in  $^{34}_{12}\text{Mg}$  and  $^{100}_{40}\text{Zr}$ , suggesting sizable influence of the pairing on the HF configurations as discussed in Subsec. III A.

For the HF (viz.  $g = 0$ ) solutions, the  $D_x(2^+)$  values are negative. This means that the DoP  $\langle J | \hat{D} | J \rangle$  decreases and the nucleons slightly spread as  $J$  goes up. As  $g$  increases from the critical points,  $D_x(2^+)$  increases. The signs of  $D_x(2^+)$  change between  $g = 1.1$  and 1.2. Thus, although the nucleons spread with increasing  $J$  at the HF level, the pair



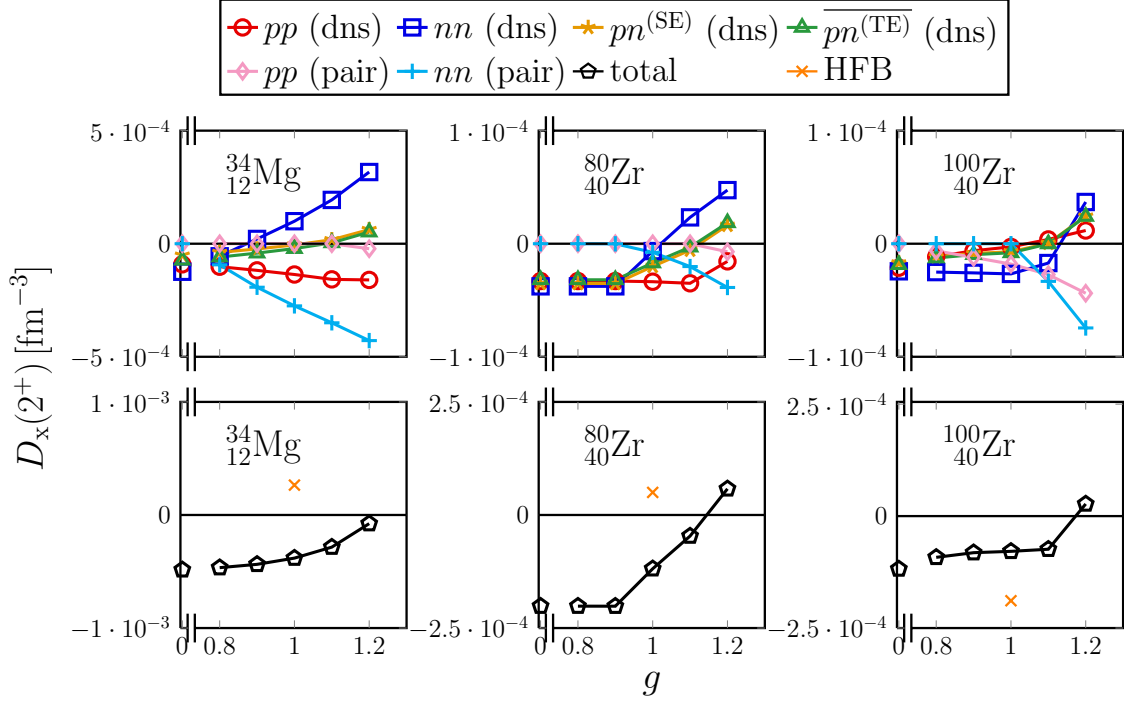


FIG. 16.  $D_x(2^+)$  in the HF+BCS solutions of  $^{34}_{12}\text{Mg}$  and  $^{80,100}_{40}\text{Zr}$ . See Fig. 15 for conventions. The orange crosses are the total values of  $D_x(2^+)$  for the HFB solutions.

correlations reduce and finally invert the effect. The  $D_x(2^+)$  values are decomposed into the individual isospin components. As  $g$  increases, contributions of  $\langle \hat{D}_{\text{dns}} \rangle$  to  $D_x(2^+)$  also increase irrespective of the four isospin components, while those of  $\langle \hat{D}_{\text{pair}} \rangle$  decrease from zero. We should note that there will be counter effects in actual nuclei that are not included in the pure rotational energy. The intrinsic state may gradually stretch with increasing  $J$ , as handled in the cranking model [3, 6, 10] and the VAP schemes [3].

These results correlate well with  $\mathcal{S}_x(2^+)/E_x(2^+)$  in Fig. 8, particularly for  $\hat{\mathcal{S}} = \hat{V}^{(C)}$  and  $\hat{V}^{(C\rho)}$ . This correlation seems to reflect the short-range nature of the nucleonic interaction. It is interpreted that the contributions of the individual components of the interaction to the rotational energy are governed by the spatial proximity among constituent nucleons measured by the DoP. Although the proximity changes with  $J$  only by a small fraction, its effects on the pure rotational energy are significant. This argument is supported by comparing the fraction with those for  $\hat{V}^{(C)}$  and  $\hat{V}^{(C\rho)}$ , *i.e.*, the percentage of the contribution to the rotational energy in the whole  $\hat{V}^{(C)}$  and  $\hat{V}^{(C\rho)}$ . If we estimate it through  $\mathcal{S}_x(2^+)/\langle 0|\hat{\mathcal{S}}|0\rangle$  and take  $^{80}_{40}\text{Zr}$  as an example, the value is  $3.1 \times 10^{-5}$  ( $1.8 \times 10^{-5}$ ) for  $\hat{\mathcal{S}} = \hat{V}^{(C)}$  ( $\hat{\mathcal{S}} = \hat{V}^{(C\rho)}$ ).

The corresponding value for the DoP ( $\hat{S} = \hat{D}$ ) is  $1.5 \times 10^{-5}$ . The ratios with the same order of magnitude are compatible with the interpretation that the DoP plays an essential role in the contribution of the nucleonic interaction to the rotational energy. The consequence also applies to the HF results reported in Ref. [23], and to the effects of the pairing. When the DoP diminishes (*i.e.*, the constituent nucleons tend to spread) for increasing  $J$ , the attractive (repulsive) forces like  $\hat{V}^{(C)}$  ( $\hat{V}^{(C\rho)}$ ) increase (decrease) the rotational energy, and *vice versa*, mediated by the overlap functions.

#### IV. CONCLUSION

The pure rotational energy of nuclei, *i.e.*, the rotational energy for a fixed intrinsic state, has extensively been analyzed by applying the AMP to the self-consistent axial-MF solutions with the semi-realistic effective Hamiltonian M3Y-P6. The contributions of the constituent terms of the Hamiltonian to the total rotational energies have been inspected, focusing on effects of the pairing.

Due to the pair correlations, the compositions of the pure rotational energy drastically change, sometimes inverting their signs, and depend strongly on nuclides even for the well-deformed nuclei. When the pairing becomes stronger, the contributions of the kinetic energies increase. Those of the attractive (repulsive) forces decrease (increase), and their signs could invert.

The degree of proximity (DoP) between nucleons slightly depends on the angular momentum  $J$ , and could account for the effects of nucleonic interactions on the rotational energy. The nucleons slightly spread as  $J$  increases at the HF level, while the pair correlations can reduce or invert the effect. It is concluded that the rotational energy of nuclei is carried by the kinetic energy in its major part, but is contributed by the nucleonic interaction as well, sensitively reflecting the DoP, *i.e.*, the degree how frequently two constituent nucleons come close. This spatial correlation accounts for the stable composition of the pure rotational energy in the HF states of well-deformed medium-to-heavy nuclei found in Ref. [23], the deviation in light nuclei and weakly-deformed states, and the disarrangement due to the pairing. For actual nuclei, the intrinsic state varies as  $J$  increases, and this effect influences the DoP and the rotational energy, which is ignored in the present study and left for future works. Still, even when the intrinsic state depends on  $J$ , the role of the DoP discovered here

will give us an insight into the effects of the interaction on the rotational energy of nuclei.

## ACKNOWLEDGMENTS

The authors are grateful to H. Kurasawa, K. Yoshida and K. Washiyama for discussions. A part of this work was performed under the long-term international workshop on “Mean-field and Cluster Dynamics in Nuclear Systems (MCD2022)”, sponsored by the Yukawa International Program for Quark-Hadron Sciences and held at Yukawa Institute for Theoretical Physics (YITP), Kyoto University, Japan. This research was partly supported by the research assistant program at Chiba University. Numerical calculations were carried out on Yukawa-21 at YITP, Oakforest PACS at Center for Computational Sciences, University of Tsukuba under the Multidisciplinary Cooperative Research Program, and HITACHI SR24000 at the Institute of Management and Information Technologies, Chiba University.

- 
- [1] A. Bohr and B. R. Mottelson, *Nuclear Structure*, Vols. I, II (World Scientific, Singapore, 1998).
  - [2] National Nuclear Data Center, <https://www.nndc.bnl.gov/>.
  - [3] P. Ring and P. Schuck, *The Nuclear Many-Body Problem* (Springer-Verlag, Berlin, 1980).
  - [4] R. E. Peierls and J. Yoccoz, Proc. Phys. Soc. London, Sect. A **70**, 381 (1957).
  - [5] J. Yoccoz, Proc. Phys. Soc. London, Sect. A **70**, 388 (1957).
  - [6] R. E. Peierls and D. J. Thouless, Nucl. Phys. **38**, 154 (1962).
  - [7] B. J. Verhaar, Nucl. Phys. **45**, 129 (1963).
  - [8] B. J. Verhaar, Nucl. Phys. **54**, 641 (1964).
  - [9] N. Onishi and S. Yoshida, Nucl. Phys. **80**, 367 (1966).
  - [10] A. Kamlah, Z. Phys. **216**, 52 (1968).
  - [11] R. Balian and E. Brezin, Nuov Cim. B **64**, 37 (1969).
  - [12] H. J. Mang, Phys. Rep. **18**, No. 6, 325 (1975).
  - [13] K. Hara and S. Iwasaki, Nucl. Phys. **A332**, 61 (1979).
  - [14] K. Hara, S. Iwasaki and K. Tanabe, Nucl. Phys. **A332**, 69 (1979).
  - [15] K. Hara and S. Iwasaki, Nucl. Phys. **A348**, 200 (1980).
  - [16] P. R. Rodríguez-Guzmán, J. L. Egido and L. M. Robledo, Nucl. Phys. A **709**, 201 (2002).

- [17] M. Bender, P. H. Heenen and P. G. Reinhard, *Rev. Mod. Phys.* **75**, 121 (2003).
- [18] K. W. Schmid, *Prog. Part. Nucl. Phys.* **52**, 565 (2004).
- [19] M. Bender and P. H. Heenen, *Phys. Rev. C* **78**, 024309 (2008).
- [20] L. M. Robledo, T. R. Rodríguez and P. R. Rodríguez-Guzmán, *J. Phys. G: Nucl. Part. Phys.* **46**, 013001 (2019).
- [21] B. Bally and M. Bender, *Phys. Rev. C* **103**, 024315 (2021).
- [22] J. A. Sheikh, J. Dobaczewski, P. Ring, L. M. Robledo and C. Yannouleas, *J. Phys. G: Nucl. Part. Phys.* **48**, 123001 (2021).
- [23] K. Abe and H. Nakada, *Phys. Rev. C* **106**, 054317 (2022).
- [24] D. J. Thouless and J. G. Valatin, *Nucl. Phys.* **31**, 211 (1962).
- [25] S. T. Belyaev, *Mat. Fys. Medd. Dan. Vid. Selsk.* **31**, No. 11 (1959).
- [26] D. R. Inglis, *Phys. Rev.* **96**, 1059 (1954); **97**, 701 (1955).
- [27] B. R. Mottelson and J. G. Valatin, *Phys. Rev. Lett.* **5**, 511 (1960).
- [28] H. Nakada, *Phys. Rev. C* **68**, 014316 (2003).
- [29] H. Nakada, *Phys. Rev. C* **87**, 014336 (2013).
- [30] H. Nakada, *Int. J. Mod. Phys. E* **29**, 1930008 (2020).
- [31] G. Bertsch, J. Borysowicz, H. McManus and W. G. Love, *Nucl. Phys. A* **284**, 399 (1977).
- [32] W. N. Cottingham, M. Lacombe, B. Loiseau, J. M. Richard and R. Vinh Mau, *Phys. Rev. D* **8**, 800 (1973).
- [33] M. Lacombe, B. Loiseau, J. M. Richard, R. Vinh Mau, J. Côté, P. Pirés and R. de Tournell, *Phys. Rev. C* **21**, 861 (1980).
- [34] N. Anantaraman, H. Toki and G. F. Bertsch, *Nucl. Phys. A* **398**, 269 (1983).
- [35] D. Davesne, A. Pastore and J. Navarro, *Prog. Part. Nucl. Phys.* **120**, 103870 (2021).
- [36] H. Nakada and K. Sugiura, *Prog. Theor. Exp. Phys.* **2014**, 033D02 (2014); **2016**, 099201 (2016).
- [37] Y. Suzuki, H. Nakada and S. Miyahara, *Phys. Rev. C* **94**, 024343 (2016).
- [38] S. Miyahara and H. Nakada, *Phys. Rev. C* **98**, 064318 (2018).
- [39] M. Matsuo, K. Mizuyama and Y. Serizawa, *Phys. Rev. C* **71**, 064326 (2005).
- [40] D. A. Varshalovich, A. N. Moskalev and V. K. Khersonskii, *Quantum Theory of Angular Momentum* (World Scientific, Singapore, 1988).
- [41] J. J. Sakurai, *Modern Quantum Mechanics Revised Edition* (Addison Wesley Longman, 1994).

- [42] R. Kubo, J. Phys. Soc. Jpn. **17**, No. 7, 1100 (1962).
- [43] H. Nakada and M. Sato, Nucl. Phys. A **699**, 511 (2002); **714**, 696 (2003).
- [44] H. Nakada, Nucl. Phys. A **808**, 47 (2008).
- [45] H. Nakada, Nucl. Phys. A **764**, 117 (2006); **801**, 169 (2008).
- [46] K. Neergård and E. Wüst, Nucl. Phys. A **402**, 311 (1983).
- [47] L. M. Robledo, Phys. Rev. C **79**, 021302(R) (2009).
- [48] J. W. Negele and H. Orland, *Quantum Many-Particle Systems* (Addison-Wesley, 1995).
- [49] G. F. Giuliani and G. Vignale, *Quantum Theory of the Electron Liquid* (Cambridge Univ. Press, Cambridge, 2005).
- [50] P. Doornenbal, H. Scheit, S. Takeuchi, N. Aoi, K. Li, M. Matsushita, *et al.*, Phys. Rev. Lett. **111**, 212502 (2013).
- [51] T. Sumikama, K. Yoshinaga, H. Watanabe, S. Nishimura, Y. Miyashita, K. Yamaguchi, *et al.*, Phys. Rev. Lett. **106**, 202501 (2011).
- [52] N. Paul, A. Corsi, A. Obertelli, P. Doornenbal, G. Authelet, H. Baba, *et al.*, Phys. Rev. Lett. **118**, 032501 (2017).
- [53] C. J. Lister, M. Campbell, A. A. Chishti, W. Gelletly, L. Goettig, R. Moscrop, *et al.*, Phys. Rev. Lett. **59**, 1270 (1987).
- [54] T. Baumann, A. M. Amthor, D. Bazin, B. A. Brown, C. M. Folden III, A. Gade, *et al.*, Nature **449**, 1022 (2007).
- [55] H. Nakada and K. Takayama, Phys. Rev. C **98**, 011301(R) (2018).
- [56] H. L. Crawford, P. Fallon, A. O. Macchiavelli, P. Doornenbal, N. Aoi, F. Browne, *et al.*, Phys. Rev. Lett. **122**, 052501 (2019).